Extracellular Vesicles Deliver Mitochondria and HSP27 Protein to Protect the Blood-Brain Barrier

Kandarp M. Dave[1], Donna B. Stolz[2], Michael John Reynolds[3], Riyan Babidhan[1], Duncan X. Dobbins[1], Hannah Yankello[4], Rohan Reddy[1], Younsoo Bae[5], Sruti S. Shiva[3,6], Devika S Manickam[1]

[1]Graduate School of Pharmaceutical Sciences, Duquesne University, Pittsburgh, PA

[2]Center for Biologic Imaging, University of Pittsburgh Medical School, Pittsburgh, PA

[3]Pittsburgh Heart Lung Blood Vascular Institute, University of Pittsburgh Medical School, Pittsburgh, PA

[4]Departments of Chemical and Biomedical Engineering, Carnegie Mellon University, Pittsburgh, PA

[5]Department of Pharmaceutical Sciences, College of Pharmacy, The University of Kentucky, Lexington, KY

[6]Department of Pharmacology & Chemical Biology, University of Pittsburgh Medical School, Pittsburgh, PA

†Corresponding author:

Devika S Manickam, Ph.D.

600 Forbes Avenue, 453 Mellon Hall

Pittsburgh, PA 15282.

Email: soundaramanickd@duq.edu, Twitter: @manickam_lab

Phone: +1 (412) 396-4722, Fax +1 (412) 396-2501

Highlights

- Small and medium-to-large extracellular vesicles (sEVs and m/lEVs) were studied
- m/lEVs have a greater mitochondrial load and increase mitochondrial function
- m/lEV mitochondria colocalized with mitochondria in recipient brain endothelial cells
- EV/HSP27 mixtures decreased dextran permeability in brain endothelial cells (BECs)
- A combination of EV mitochondria and exogenous HSP27 mitigates BEC ischemic damage

Abstract

Ischemic stroke causes brain endothelial cell death and damages tight junction integrity of the blood-brain barrier (BBB). We engineered endothelial cell-derived extracellular vesicles (EVs) for the delivery of exogenous heat shock protein 27 (HSP27) and harnessed the innate EV mitochondrial load as a one-two punch strategy to increase brain endothelial cell survival (via mitochondrial delivery) and preserve their tight junction integrity (via HSP27 delivery). We demonstrated that the medium-to-large (m/lEV) but not small EVs (sEV) transferred their mitochondrial load that subsequently colocalized with the mitochondrial network of the recipient primary human brain endothelial cells. This mitochondrial transfer increased the relative ATP levels and mitochondrial function in the recipient endothelial cells. EV/HSP27 mixtures decreased the paracellular permeability of small and large molecular mass fluorescent tracers in oxygen glucose-deprived primary human brain endothelial cells. This one-two punch approach to increase the metabolic function and structural integrity of brain endothelial cells is a promising strategy for BBB protection and prevention of long-term neurological dysfunction post-ischemic stroke.

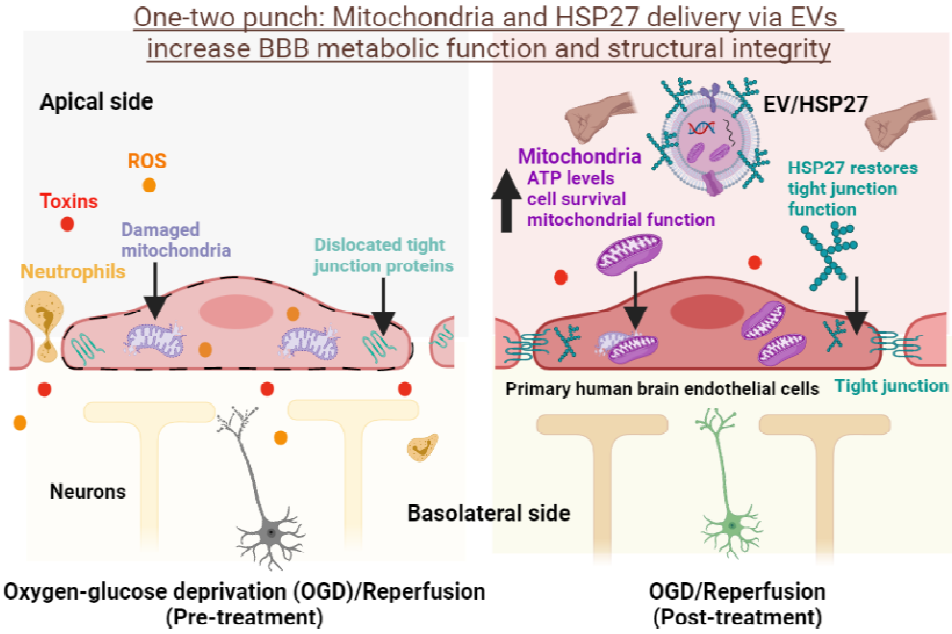

Graphical Abstract

Keywords

extracellular vesicles, mitochondria, heat shock protein, paracellular permeability, BBB protection, ischemic stroke

Abbreviations

ATP	Adenosine triphosphate
BBB	Blood-brain barrier
BECs	Brain endothelial cells
Calcein AM	Calcein acetoxymethyl
ECAR	Extracellular acidification rate
EVs	Extracellular vesicles
EXOs	Exosomes
FT cycle	Freeze/Thaw cycle
GAPDH	Glyceraldehyde 3-phosphate dehydrogenase
HSP27	Heat shock protein 27
hCMEC/D3	human cerebral microvascular endothelial cell line
HBMEC	primary human brain microvascular endothelial cells
HEPES	2-Hydroxyethylpiperazine-N'-2-Ethanesulfonic Acid
MVs	Microvesicles
m/lEV	medium-to-large EVs
MitoT-red-EV	Mitotracker deep red-labeled extracellular vesicles
OCR	Oxygen consumption rate
OGD	Oxygen-glucose deprivation
OGD/RP	Oxygen-glucose deprivation/reperfusion
PEI	Polyethylenimine
PEG-DET	poly (ethylene glycol)-*b*-poly (diethyl triamine)
ROS	Reactive oxygen species

sEV	small EVs
TRITC	Tetramethyl rhodamine iso-thiocyanate

1. Introduction

Acute ischemic stroke is a major cause of death worldwide with recurrence and mortality rates of one stroke per 40 seconds and four deaths per minute, respectively, in the United States of America (1). During the onset of ischemic stroke, the blood flow to a brain artery is obstructed due to blood clots and plaque formation, which leads to long-term neurological damage and dysfunction or even death (2). The lack of blood supply to the affected brain area causes the deprivation of vital ions, oxygen, and nutrients consequently resulting in sudden cellular energy failure, neuron depolarization, reactive oxygen species-mediated cell death, and blood-brain barrier (BBB) dysfunction (2-4). Alteplase (recombinant tissue plasminogen activator) is the only FDA-approved treatment for ischemic stroke which dissolves the blood clot and restores the blood flow (5). However, its narrow therapeutic window (<4.5 h of onset) limits its use to only about 5% of patients (4). Importantly, the reestablishment of blood flow in the affected brain area outside its therapeutic window contributes to the influx of water and osmotic solutes through the damaged BBB (ischemia/reperfusion) and consequently, aggravates the BBB breakdown and risk of hemorrhagic transformation (4, 6). The limited therapeutic options and the associated severe side effects associated with Alteplase drive the development of safe and efficient stroke therapeutics.

Oxygen and glucose deprivation (OGD) in ischemic stroke reduce ATP levels in the endothelial cells lead to impaired functionality of Na^+-K^+-ATPase and Ca^{2+} ATPase activity which accumulates these cations within the cells (3, 4). This further leads to Na^+ and water influx that causes endothelial swelling and breakdown of the BBB. Na^+ accumulation-mediated depolarization of endothelial plasma membrane also rapidly increases intracellular Ca^{2+} and

activates the release of excitatory neurotransmitters such as glutamate and dopamine (7). Intracellular calcium overload catalyzes enzymatic activities leading to protein degradation, DNA damage, generation of reactive oxygen species (ROS), mitochondrial dysfunction, and the subsequent impairment of mitochondrial ROS defense mechanisms. Overall, hypoperfusion in the ischemic brain region leads to a rapid decrease in endothelial ATP levels, endothelial swelling, and mitochondrial dysfunction. Therefore, restoring the endothelial bioenergetics and mitochondrial function is a viable strategy to rescue ischemic endothelial cell death. In addition, disruption of the BBB is a major hallmark of ischemic stroke that is associated with altered expression of tight junctions, adherens junction proteins, and BBB transporters (2-4). Early ischemia/reperfusion activates the polymerization of the actin cytoskeleton in endothelial cells which triggers the formation of F-actin and myosin-containing contractile stress-fibers. These force-generating fibers transmit tension to the tight and adherens junction proteins which disassemble and internalize the tight junction proteins and consequently lead to the loss of barrier properties of the endothelial cells lining the BBB (8, 9). Uncontrolled actin polymerization-induced breakdown of BBB leads to infiltration of proinflammatory mediators, blood cells, circulatory immune cells, and toxins into the brain parenchyma, and lead to the secondary injury cascade (9, 10). Hence, a combined strategy to increase the endothelial cell bioenergetics to decrease cell death and reduce their paracellular permeability, ultimately leading to protection of BBB integrity is a viable approach for the treatment of ischemia/reperfusion injury.

Preclinical studies have demonstrated that endothelial, but not neuronal overexpression of heat shock protein 27 (HSP27), inhibited actin polymerization and elicited long-lasting protection against ischemia/reperfusion-induced BBB disruption and neurological deficits (9,

10). Lower endothelial HSP27 levels increase BBB permeability and slow down the recovery of the damaged BBB under pathological conditions (11). HSP27 binds to actin monomer and also sequesters globular-actin (G-actin) monomer in the endothelial cells that prevents the binding of G-actin to filamentous-actin (F-actin) and further inhibits tight junctional protein translocation in endothelial cells (9, 11-14). HSP27 (24-27 kD) is a highly conserved molecular chaperone from a small HSP family (15) and has multiple functionalities including suppression of caspase activation (16, 17), inhibition of cytochrome release (18), and reduction of protein aggregation. Intravenous administration of cell-penetrating transduction domain (TAT)-HSP27 rapidly enhanced HSP27 levels in brain microvessels and reduced infract volume as well as ischemia/reperfusion-induced BBB disruption (9). However, the systemic delivery of HSP27 using cationic TAT peptide resulted in non-specific uptake-associated side effects in the brain and other tissues (9). Therefore, the delivery of exogenous human recombinant HSP27 protein to the brain endothelial cells (BECs) using natural carriers like extracellular vesicles (EVs) can likely increase its specific uptake into BECs owing to inherent membrane affinity of BEC-derived EVs to parent/donor BECs (19, 20).

EVs are an emerging class of natural nanocarriers for biotherapeutics due to their known roles in intercellular communication, lower immunogenicity, and inherent homing capabilities to target cells (21, 22). The smaller EVs (sEVs) range from 30-200 nm in particle diameter and their biogenesis involves the inward budding of endosomal membranes that transforms into multivesicular bodies (MVBs) followed by their fusion with the plasma membrane and sEV release into extracellular spaces (22). The biogenesis of the medium-to-larger EVs (m/lEVs) involves their outward budding from the cell's plasma membrane with particle diameters ranging

from 100 – 1000 nm (22). The selective packaging of the functional mitochondria and mitochondrial proteins in the MVs can increase the bioenergetics of recipient cells by releasing their vesicular components, including mitochondria, nucleic acids, proteins, and lipids. Mitochondria play a central role in cellular energy production and regulation of cell death including apoptosis and autophagy (24). Ischemia-induced mitochondrial dysfunction initiates the generation of excessive reactive oxygen species, reduction in ATP levels, and consequently cellular and neuronal death (24). Therefore, protection of mitochondrial function via exogenous functional mitochondria supplementation is an exciting strategy to increase endothelial cell survival post-ischemic stroke. Thus, we rationalize that mitochondria-rich MVs derived from brain endothelial cells can increase cellular bioenergetics and survival under normoxic and hypoxic conditions.

Surface engineering of BEC-derived EVs with exogenous HSP27 is a promising strategy that can allow harnessing the inherent targeting capabilities of the EVs to the recipient BECs along with the added benefits of their mitochondrial load. Alongside BEC-derived EVs, we have also tested the capability of a synthetic cationic polymer, poly (ethylene glycol)-*b*-poly (diethyltriamine) (PEG-DET) to formulate and deliver HSP27. We have previously used PEG-DET polymer to form nanosized complexes with superoxide dismutase protein and demonstrated a >50% reduction in brain infract volume in a mouse model of acute ischemic stroke (25). PEG-DET is a cationic diblock copolymer known for its safety and gene transfer efficacy in comparison to commercial transfection agents such as lipofectamine, polyethyleneimine, and other cationic polymers (26-28).

Here, we *hypothesize* that the engineering of innate mitochondria-containing BEC-derived EVs with exogenous HSP27 protein is one double-punch approach to increase BEC survival (via mitochondrial delivery) and preserve its tight junction barrier via decreasing the paracellular permeability (via HSP27 delivery) of the endothelial monolayers post-ischemia. This approach will protect and strengthen the BBB that in turn can ameliorate the long-term neurological damage and dysfunction.

In this study, we isolated sEV and m/lEV from hCMEC/D3: a human brain endothelial cell line using a sequential ultracentrifugation method (29) and characterized their particle diameter, zeta potential, and membrane integrity post-cold storage. While we collectively refer to both large (m/lEV) and small (sEV) vesicle fractions as EVs, we have studied the singular effects of both m/lEVs and sEVs. We demonstrated the presence of mitochondria in m/lEV sections using transmission electron microscopy. We evaluated the effects of EV dose and incubation times on mitochondrial transfer to the recipient cells and demonstrated the integration of MV-delivered mitochondria with the mitochondrial network of the recipient endothelial cells. We studied the effects of EV exposure on the resulting relative ATP levels, mitochondrial respiration, and glycolytic capacity of the recipient endothelial cells under normoxic and hypoxic conditions. The formation of EV/HSP27 and PEG-DET/HSP27 complexes/mixtures and their physicochemical characteristics were confirmed using native polyacrylamide gel electrophoresis and dynamic light scattering. The cytocompatibility of EV/HSP27 mixtures and PEG-DET/HSP27 complexes were evaluated using an ATP assay. The effects of HSP27 delivery on the paracellular permeability of small and large molecule fluorescent tracers were evaluated under ischemic and ischemia/reperfusion conditions in primary human brain endothelial cultures.

2. Materials

Recombinant human HSP27 was purchased from Novus Biologicals (Centennial, CO). Cell Titer Glo 2.0 reagent (ATP assay) was procured from Promega (Madison, WI). Micro BCA and Pierce BCA protein assay kits were purchased from Thermo Scientific (Rockford, IL). PEG-DET polymer was synthesized by aminolysis of PEG-poly(β-benzyl L-aspartate) block copolymers with diethyltriamine as previously reported (26, 28, 30, 31). Bio-Safe Coomassie G-250 stain was purchased from Bio-Rad Laboratories Inc. (Hercules, CA). Collagen Type I was purchased from Corning (Discovery Labware Inc, Bedford, MA) and endothelial cell basal medium-2 (EBM-2) was procured from Lonza (Walkersville, MD). Hydrocortisone, human basic fibroblast growth factor and ascorbic acid were purchased from Sigma-Aldrich (Saint Louis, MO). Penicillin-Streptomycin solution and Chemically Defined Lipid Concentrate were procured from Invitrogen (Carlsbad, CA). Heat-inactivated fetal bovine serum was bought from Hyclone Laboratories (Logan, UT). Polycarbonate centrifuge tubes were purchased from Beckman Coulter, Inc. (Brea, CA). Electrophoresis sample buffer was purchased from Bio-Rad (Hercules, CA). RIPA buffer was procured from Alfa Aesar (Ward Hill, MA). PET track-etched membrane Falcon Cell Culture inserts of 0.4 µm pore size were procured from Corning (Discovery Labware Inc, Bedford, MA). TRITC 65-85 kD and 4.4 kD dextran was procured from Sigma (St. Louis, MO). A low-volume disposable cuvette (Part no. ZEN0040, Malvern) was used for particle size measurements. CellLight Mitochondria-GFP Backman 2.0 reagent, MitoTracker Green FM, and MitoTracker Deep Red FM, Dynabeads Protein G (cat#10003D), and DynaMag-2 magnetic stand (cat#12321D) were procured from Invitrogen (Eugene, OR). Mouse monoclonal antibodies against ATP5A, GAPDH, HSP27 were purchased from Abcam. Mouse monoclonal antibody

against CD9 was received from Life Technologies corporation (Eugene, OR), whereas Alexa Fluor 790-conjugated donkey anti-mouse IgG was received from Jackson ImmunoResearch Lab Inc (West Grove, PA).

2.1. Cell models

A human cerebral microvascular endothelial cell line (hCMEC/D3, catalog number. 102114.3C) was received from Cedarlane Laboratories (Burlington, Ontario) at passage number (P) 25, and cells between P25 and P35 were used in all experiments (19, 29). hCMEC/D3 cells were grown in tissue culture flasks, multiwell plates, or transwell inserts pre-coated using 0.15 mg/mL rat collagen I in a humidified 5% CO_2 incubator at 37 ± 0.5˚C (Isotemp, Thermo Fisher Scientific). The cells were cultured in complete growth medium composed of endothelial cell basal medium (EBM-2) supplemented with fetal bovine serum (5% FBS), penicillin (100 units/mL)-streptomycin (100 µg/mL) mixture, hydrocortisone (1.4 µM), ascorbic acid (5 µg/mL), Chemically Defined Lipid Concentrate (0.01%), 10 mM HEPES (pH 7.4), and bFGF (1 ng/mL). The complete growth medium was replenished every other day until the cells formed confluent monolayers. Prior to passage, the cells were washed using 1x phosphate buffer saline (PBS) and detached from the flask using 1x TrypLE Express Enzyme (gibco, Denmark). We received primary human brain microvascular endothelial cells (HBMEC, catalog no. ACBRI 376) from Cell Systems (Manassas, VA) at P3, and cells below P11 were used in all experiments. HBMECs maintained in Cell Systems Classic Culture Medium containing 1% culture boost were cultured in tissue culture flasks, multiwell plates, or transwell inserts pre-treated with attachment factors. The complete growth medium was replenished every day until the cells formed confluent monolayers. For passage, HBMEC monolayers were washed with

Passage Reagent Group 1 (PRG 1, dPBS/EDTA solution), detached with PRG 2 (dPBS/trypsin-EDTA solution) and PRG 3 (trypsin inhibitor solution).

2.2. Isolation of sEVs and m/lEVs from hCMEC/D3 cells

It should be noted that while we collectively refer to both large (m/lEV) and small (sEV) vesicle fractions as EVs, we study both m/lEV and sEV. Wherever noted, a 1:1 w/w mixture of sEV and m/lEV is collectively referred to as EVs. sEV and m/lEV were isolated from conditioned medium supernatants of hCMEC/D3 cells using the differential ultracentrifugation method (29). Briefly, tissue culture flasks with 175 cm^2 growth area (T175) containing confluent hCMEC/D3 were washed with pre-warmed 1x PBS and incubated with serum-free medium for 48 h in a humidified 5% CO_2 incubator at 37 ± 0.5˚C. Post-incubation, the EV-conditioned medium was collected in polypropylene centrifuge tubes and centrifuged at 2000 ×g for 22 min at 4°C to pellet down apoptotic bodies and cell debris using a Sorvall ST 8R centrifuge (ThermoFisher Scientific, Osterode am Harz, Germany). The supernatant was transferred into polycarbonate tubes and centrifuged at 20,000 ×g for 45 min at 4°C to pellet down m/lEV using an Optima XE-90 ultracentrifuge equipped with a 50.2 Ti rotor (Beckman Coulter, Indianapolis, IN). Next, the supernatant was filtered through a 0.22 µm PES membrane syringe filter, and the flow-through was centrifuged at 120,000 ×g for 70 min at 4°C to collect EXOs. Lastly, m/lEV and sEV pellets were washed with 1x PBS and suspended in either 1x PBS for particle diameter measurements and *in vitro* experiments or 10 mM HEPES buffer pH 7.4 for zeta potential measurements. sEV and m/lEV samples were stored at -80°C until further use. The total protein content in sEV and m/lEV was quantified using Pierce MicroBCA assay. Briefly, sEV and m/lEV were lysed with 1x RIPA buffer containing 3 µg/mL aprotinin at a 1:15 v/v ratio.

Following that, a 150 µL volume of sEV/m/lEV lysates or BSA standards (0.5–200 µg/mL) was pipetted into a 96-well plate and an equal volume of the MicroBCA working reagent (reagent A: reagent B: reagent C at 25:24:1 volume ratio) was added to each well. The reagent mixture was incubated at 37 °C for 2 h and the absorbance was measured at 562 nm using a SYNERGY HTX multi-mode reader (BioTek Instruments Inc., Winooski, VT).

2.3. Dynamic light scattering (DLS)

The stability of naïve EVs under storage conditions was determined by their measuring particle diameter and zeta potential using dynamic light scattering. EV samples at 0.5 mg protein/mL in 1x PBS were frozen at -20°C for 24 h and thawed at room temperature for 30 min. Post-thawing, the particle diameters, and dispersity indices were measured using Malvern Zetasizer Pro (Worcestershire, UK). The freeze-thaw (FT) cycle was repeated three times and all samples were run in triplicate. Average particle diameter, dispersity index, and zeta potential values were reported as mean ± standard deviation.

2.4. Membrane integrity of EVs after isolation and upon storage conditions

The membrane integrity of sEV and m/lEV post-isolation and upon revival after their storage conditions (described earlier in the DLS section) was determined using a calcein AM flow cytometry assay. First, polystyrene sub-micron-sized beads ranging from 0.2 – 2 µm particle diameters were used to calibrate the Attune NxT flow cytometer. The calibration beads, sEV, and m/lEV samples were tested and events captured in forward scatter (FSC) and side scatter (SSC) plots were analyzed using a small particle side scatter 488/10-nm filter (BL1) channel. sEV and m/lEV were diluted to 20 µg protein/mL in PBS and incubated/stained with 10 µM

calcein AM for 20 min at room temperature in the dark. Unstained sEV and m/lEV were used to gate the background signals, whereas samples treated with 2% v/v Triton X-100 followed by staining with calcein AM were used as controls to determine if calcein-positive signals were specifically associated with intact EVs. For each sample analysis, an aliquot of 100 µL was run through Attune NxT Acoustic cytometer (Invitrogen, Singapore) and 50,000 events were recorded during the run. The calcein-associated fluorescence intensity was detected at 488/10 nm and percentage signal intensities were presented in histogram plots generated using Attune software. Calcein AM-associated background signals were gated using the controls such as PBS containing 10 µM calcein AM and PBS/2% Triton X-100/calcein AM mixture.

2.5. Transmission Electron Microscopy analysis of EVs

EVs were loaded on Formvar/carbon-coated grids, negatively stained with 1% uranyl acetate and examined with a JEM-1400 Plus transmission electron microscope (JEOL, Peabody, MA, USA) fitted with an AMT digital camera (Danvers, MA, USA) (32). Suspensions of EVs were pelleted at 100,000xg in a Beckman airfuge for 20 min and the pellets were fixed in 2.5% glutaraldehyde in PBS overnight. The supernatant was removed and the cell pellets were washed 3x in PBS and post-fixed in 1% OsO_4, 1% $K_3Fe(CN)_6$ for 1 hour. Following 3 additional PBS washes, the pellet was dehydrated through a graded series of 30-100% ethanol. After several changes of 100% resin over 24 hours, pellet was embedded in a final change of resin, cured at 37°C overnight, followed by additional hardening at 65°C for two more days. Ultrathin (70 nm) sections were collected on 200 mesh copper grids, stained with 2% uranyl acetate in 50% methanol for 10 minutes, followed by 1% lead citrate for 7 min. Sections were imaged using a

JEOL JEM 1400 Plus transmission electron microscope (Peabody, MA) at 80 kV fitted with a side mount AMT 2k digital camera (Advanced Microscopy Techniques, Danvers, MA).

2.6. Uptake of Mitotracker-labeled EVs into hCMEC/D3 cells using flow cytometry

2.6.1. Isolation of mitochondria-labeled EVs

hCMEC/D3 cells (P32) were cultured in a T175 flask to confluency. The complete growth medium was removed, cells were washed with 1x PBS, and cells were incubated with 100 nM Mitotracker deep red (MitoT-red) diluted in a conditioned medium for 30 min in a humidified incubator. Next, the medium was replaced with serum-free medium after washing the cells with 1x PBS, and cells were kept in a humidified incubator for 24 h. Post-incubation, the conditioned medium was collected into centrifuge tubes. sEV (MitoT-red-sEV) and m/lEV (MitoT-red-m/lEV) from Mitotracker Red-labeled cells were isolated from the conditioned medium using the differential centrifugation method described in section 2.2. The EV protein content in MitoT-red-sEV and MitoT-red-m/lEV were determined using MicroBCA assay and the samples were stored at -80 °C until further use. For the EVs labeled post-isolation, EVs were incubated with MitoT-red to stain the polarized mitochondria, and the EV pellets were washed using 1*x* PBS to remove excess/free MitoT-red dye.

2.6.2. Quantification of EV-mediated mitochondria transfer into recipient hCMEC/D3 cells using flow cytometry

hCMEC/D3 cells were cultured in 48-well plates at 50,000 cells/well in complete growth medium. Unstained and untreated cells were used as a control, whereas cells stained with 250 nM of Mitotracker deep red (MitoT-red) for 45 min in complete growth medium were used as a

positive control. The cells were treated with MitoT-red-sEV and MitoT-red-m/lEV at 30, 75, and 150 µg EV protein/well in complete growth medium for 72 h in a humidified incubator. The cells were also treated with unlabeled sEV and m/lEV at 150 µg EV protein/well in complete growth medium for 72 h. Post-treatment, the cells were washed with 1x PBS, dissociated using TrypLE Express, diluted with PBS, and collected into centrifuge tubes. For each sample, an aliquot of a 100 µL cell suspension was analyzed through Attune NxT Flow cytometer and 10,000 events were recorded in FSC vs. SSC plots. The Mitotracker deep red fluorescence intensity was detected at 670/14 nm and percentage signal intensities were presented in histogram plots generated using Attune software version 3.2.3. Mitotracker deep red background signals were gated using the controls including PBS and untreated cells.

2.7. Uptake of Mitotracker-labeled EVs into primary human brain endothelial cells using fluorescence microscopy

2.7.1. Uptake of MitoT-red-EXOs and MitoT-red-MVs into primary HBMEC monolayers

MitoT-red sEV and MitoT-red-m/lEV were isolated from the conditioned medium of hCMEC/D3 cells as described in section 2.6.1. Primary HBMEC (P6) were cultured in 96-well plates at 16,500 cells/well in complete growth medium. Post-confluency, the cells were treated with MitoT-red-sEV and MitoT-red-m/lEV at 10, 25, and 50 µg EV protein/well in complete growth medium for 24, 48, and 72 h in a humidified incubator. At each time-point, the cells were observed under an Olympus IX 73 epifluorescent inverted microscope (Olympus, Pittsburgh, PA) using the Cyanine-5 (Cy5, excitation 651 nm, and emission 670 nm) and bright-field channels at 20x magnification. Images were acquired using CellSens Dimension software (Olympus, USA).

2.7.2. Colocalization of EV-mitochondria with the mitochondrial network in the recipient hCMEC/D3 and HBMEC monolayers

2.7.2.1. Mitotracker green staining of recipient cell mitochondria

HBMEC and hCMEC/D3 cells were seeded in a 96 well-plate at 16,500 cells/well and incubated in a humidified incubator at 37°C. Post-confluency, the complete growth medium was removed, cells were washed with 1x PBS, and cells were incubated with 250 µM of Mitotracker green in a complete medium for 30 min. Post-treatment, the medium was replaced, washed with PBS, and incubated with MitoT-red-sEV or MitoT-red-m/lEV at 50 µg EV protein/well in a complete growth medium for 72 h in a humidified incubator. hCMEC/D3 cells stained with only Mitotracker green were used as a control. Post-incubation, the medium was removed, cells were washed and incubated with phenol-red free and serum-containing DMEM-high glucose medium. The cells were then observed under an Olympus IX 73 epifluorescent inverted microscope (Olympus, Pittsburgh, PA) using Cyanine-5 channel (Cy5, excitation 651 nm, and emission 670 nm) to detect MitoT-red-EV uptake and GFP channel to detect Mitotracker Green signals at 20x magnification and images were acquired using CellSens Dimension software (Olympus, USA).

2.7.2.2. Staining of a mitochondrial matrix protein in the recipient cells using CellLight Mitochondria-GFP BackMam reagent

We used CellLight Mitochondria-GFP BacMam to label a structural mitochondrial matrix protein (33). CellLight Mito-GFP is a fusion construct of the leader sequence of a mitochondrial matrix protein, E1 alpha pyruvate dehydrogenase, and emerald Green Fluorescent Protein (emGFP). HBMEC and hCMEC/D3 cells were seeded in a 96 well-plate at 16,500 cells/well and

incubated in a humidified incubator at 37°C. Post-confluency, the complete growth medium was removed, cells were washed with 1x PBS, and cells were incubated with CellLight Mitochondria-GFP reagent (at a dilution of 2 µL/10,000 cells as recommended by the manufacturer) for 16 h. Post-transduction, the medium was removed and cells were washed with 1x PBS. Next, the cells were incubated with MitoT-red-sEV and MitoT-red-m/lEV at 50 µg EV protein/well in complete growth medium for 72 h in a humidified incubator. HBMEC or hCMEC/D3 cells transduced with only CellLight Mitochondria-GFP were used as a control. Post-incubation at 24 and 72 h, the medium was removed, cells were washed and incubated with phenol-red free and serum-containing DMEM-high glucose medium. The cells were then observed under Olympus IX 73 epifluorescent inverted microscope (Olympus, Pittsburgh, PA) using Cyanine-5 channel (Cy5, excitation 651 nm, and emission 670 nm) to detect MitoT-EV uptake and GFP channel for CellLight Mitochondria-GFP signals at 20x magnification and images were acquired using CellSens Dimension software (Olympus, USA).

2.8. Effects of naïve EV treatment in primary HBMECs under normoxic and oxygen-glucose-deprived (OGD) conditions

To simulate ischemic conditions *in vitro*, hCMEC/D3 cells were exposed to different oxygen glucose-deprivation (OGD) parameters, and the resulting cell viability was evaluated using an ATP assay (29, 34, 35). hCMEC/D3 cells were cultured in 96-well plates at 16,500 cells/well. Confluent hCMEC/D3 cells were incubated with OGD medium defined as follows: 120 mM NaCl, 5.4 mM KCl, 1.8 mM $CaCl_2$, 0.8 mM $MgCl_2$, 25 mM Tris-HCl, pH 7.4 for 0.5 to 24 h in either normoxic or hypoxic conditions (36). For normoxic conditions, the culture plates were incubated in a humidified incubator with 95% air and 5% carbon dioxide whereas for hypoxic

conditions, the culture plates were incubated in an OGD chamber (Billups Rothenberg, Del Mar, CA) pre-flushed with 5% carbon dioxide, 5% hydrogen and 90% nitrogen at 37±0.5˚C. For normoxic conditions, the medium was removed and the recipient HBMEC monolayers were incubated with hCMEC/D3-derived sEV, m/lEV, and sEV+m/lEV at doses of 10, 25, and 50 µg EV protein/well in a humidified incubator for 24, 48, and 72 h. For hypoxic conditions, the medium was removed and the recipient HBMEC monolayers were incubated with hCMEC/D3-derived sEV, m/lEV, and sEV+m/lEV at doses of 10, 25, and 50 µg EV protein/well in the OGD medium and a humidified incubator for 24 h. Then, the treatment mixtures were replaced with pre-warmed complete growth medium, and an equal quantity of Cell Titer Glo 2.0 reagent was added. The plates were incubated for 15 min at RT on an orbital shaker in the dark and relative luminescence units were measured at 1 s integration time.

2.9. Measurement of mitochondrial function using Seahorse Analysis

The oxidative phosphorylation and glycolytic functions of hCMEC/D3 cells treated with EVs during normoxic conditions were evaluated using the Seahorse analysis by measuring oxygen consumption rate (OCR) and Extracellular Acidification rate (ECAR) (19, 37). hCMEC/D3 cells seeded at 20,000 cells/well were cultured in Seahorse XF96 plate for four days. The cells were incubated with hCMEC/D3-derived sEV, m/lEV, and sEV+m/lEV for 24, 48, and 72h at 3.4, 8.3, and 16.5 µg EV protein/well equivalent to 30, 75, and 150 µg EV protein/cm^2 in complete growth medium. Post-incubation, the medium was replaced with pre-warmed DMEM and subjected to Seahorse analysis (19). After measurement of baseline OCR, 2.5 µmol/L oligomycin A and 0.7 µmol/L carbonyl cyanide-p-trifluoromethoxyphenyl-hydrazone were consecutively

added to measure the proton leak and maximal OCR, respectively (37). The total protein of the cells in each well was measured using Pierce BCA assay.

2.10. Complexation of HSP27 with PEG-DET, sEV, m/lEV, and PEG-DET-EV

PEG-DET/HSP27 complexes were prepared using a rapid mixing method. A PEG-DET polymer solution prepared in 10 mM HEPES buffer, pH 7.4 was mixed with 2 µg HSP27 at PEG-DET/HSP27 w/w ratio 0.05, 0.2, 1, 5, 10, and 20:1 for 30 s. The mixture was incubated at room temperature (RT) for 30 min. For the preparation of sEV/HSP27 and m/lEV/HSP27 mixtures, hCMEC/D3-derived EVs were suspended in 1x PBS were incubated with 2 µg HSP27 at EV protein/HSP27 w/w ratios 5, 10, and 15:1 in centrifuge tubes. The mixture was vortexed for 30 s and incubated at room temperature for 30 min. To prepare (PEG-DET/HSP27)/EV complexes, PEG-DET/HSP27 complexes were prepared at 20:1 and 30:1 w/w ratios followed by incubation with 10 µg EV protein for 30 min at RT. The different complexes were characterized for electrophoretic mobility, particle diameter, and zeta potential.

2.11. Native Polyacrylamide Gel Electrophoresis (PAGE)

The complexation of HSP27 with PEG-DET, sEV, and m/lEV was confirmed using native PAGE. A polyacrylamide gel consisting of 4% and 10% of acrylamide in the stacking and resolving sections, respectively, was prepared using a gel casting assembly (Bio-Rad Laboratories Inc., Hercules, CA) (29, 34). Native HSP27, PEG-DET/HSP27, and EV/HSP27 complexes containing 2 µg of HSP27 at the indicated w/w ratios were mixed with native sample buffer and loaded into the gel lanes. Free PEG-DET polymer, naïve sEV, and m/lEV equivalent to indicated w/w ratios were used as controls. In an independent experiment, PEG-DET/HSP27

at w/w 20:1 and 30:1 was complexed with sEV, m/lEV, and EVs (sEV: m/lEV 1:1) at PEG-DET to EV protein 2:1 and 3:1 w/w ratios. The gel was run in 1x Tris-Glycine buffer, pH 8.3 at 100 V for 2 h at 2-8 °C using PowerPac Basic setup (Bio-Rad Laboratories Inc., Hercules, CA). Post-electrophoresis, the gel was washed with deionized water for 30 min and stained with 50 mL of Biosafe Coomassie blue G-250 for 1 h on an orbital shaker at room temperature. The gel was washed with deionized water for 30 min and scanned under Odyssey imager (LI-COR Inc., Lincoln, NE) at 800 nm channel and intensity setting 5. The band densities were quantified using ImageStudio 5.2 software.

2.12. Dynamic light scattering analysis of HSP27 complexes/mixtures

The average particle diameters, dispersity indices, and zeta potentials of the HSP27 complexes were analyzed using a Malvern Zetasizer Pro (Worcestershire, UK). hCMEC/D3 cell line-derived naïve EVs at 0.5 mg EV protein/mL were diluted in either 1x PBS for size and dispersity index or 10 mM HEPES buffer pH 7.4 for zeta potential measurements. In addition, particle sizes and dispersity indices of native HSP27 protein at 20 µg/mL, PEG-DET/HSP27 complexes at 10, 20, and 30:1 w/w ratios, sEV/HSP27 and m/lEV/HSP27 mixtures at 10:1 w/w ratio were measured in a low-volume disposable cuvette. Free PEG-DET equivalent to 10, 20, and 30:1 w/w ratios and naïve EVs equivalent to 10:1 w/w ratio were also analyzed. For the zeta potential of the above complexes, a 50 µL sample of complexes was further diluted in zeta cuvette containing 10 mM HEPES buffer at pH 7.4. The samples were run in triplicate. Data are presented as average particle diameter±standard deviation. The reported data are representative of 3 independent experiments.

2.13. Cytocompatibility of HSP27 complexes/mixtures with primary HBMEC and hCMEC/D3 monolayers

The cell viability of hCMEC/D3 and primary HBMEC monolayers treated with HSP27 complexes was measured using Cell Titer Glo (ATP) assay. hCMEC/D3 and HBMEC were seeded at 16,500 cells/well in a 96 well-plate and cultured in a humidified incubator at 37±0.5˚C. The growth medium was replaced with treatment mixtures containing either native HSP27, sEV/HSP27 (10:1), m/lEV/HSP27 (10:1), sEV+m/lEV at 1:1/HSP27 (10:1), or PEG-DET/HSP27 (20:1) at a dose of 2 µg HSP27 protein per well. Naïve sEV, m/lEV, equivalent amounts of sEV+m/lEV, and free PEG-DET equivalent to 20:1 in complete medium were used as controls. Polyethyleneimine (PEI) at 50 and 100 µg/mL in a complete growth medium was used as a positive control. The complexes and controls were treated for 72 h in a humidified incubator at 37±0.5˚C. Post-incubation, the ATP assay was performed using Cell Titer Glo 2.0 reagent as described earlier in section 2.8. The cell viability of HSP27 complexes treated HBMECs was calculated using Equation 1.

$$Cell\ viability\ (\%) = \frac{Relative\ light\ units\ (RLU) of\ treated\ cells}{RLU\ of\ untreated\ cells} \times 100 \qquad \text{(Equation 1)}$$

2.14. Paracellular permeability of TRITC-labeled 65-85 and 4.4 kD Dextran in HBMEC monolayers pre-treated with PEG-DET/HSP27 complexes

2.14.1 Hypoxic conditions (OGD only)

Primary HBMEC (P4-P9) in a complete growth medium were seeded at 50,000 cells/cm^2 in a 24-well format cell culture insert (insert area: 0.33 cm^2) for four days to form a complete endothelial monolayer. The medium was replaced every 48 h during this culturing period. The abluminal wells were filled with complete growth medium throughout the culturing period. The

complete growth medium was replaced with 300 µL of growth medium containing PEG-DET/HSP27 at a w/w ratio of 20:1 and a dose of 2 µg HSP27/well for 72 h. Post-treatment, the complete growth medium was replaced with 300 µL of OGD medium containing 1 µM TRITC-Dextran. The OGD medium containing 1µM TRITC-Dextran alone was used as a control. The medium containing 1µM TRITC-Dextran in complete growth medium alone was used as an additional control. The abluminal chamber was filled with 0.5 mL of fresh complete growth medium. The untreated group was incubated in a humidified incubator whereas OGD treatment groups were incubated in an OGD chamber (as described earlier in section 2.8.). The concentration of TRITC-Dextran in the abluminal medium was measured at 4, 6, and 24 h post-treatment. A 50 µL aliquot was collected at indicated time points from the abluminal side. An equal volume of fresh medium was replaced to maintain the sink conditions. The concentration of TRITC-Dextran was measured using Synergy HTX multimode plate reader at excitation 485/20 and emission 580/50 nm. The diffusion rate of TRITC-Dextran at each time point was calculated by the amount of TRITC- Dextran per surface area (0.33 cm^2) of the insert per time (30 min).

2.14.2. OGD/reperfusion

Post-24 h of OGD exposure, HBMECs in the culture inserts were washed with 1x PBS. HBMECs were incubated with a complete growth medium containing 1 µM TRITC 65-85 or 4.4 kD Dextran in a 24-well format cell culture insert for 1h – 24h (reperfusion) in a humidified incubator. The abluminal chamber was filled with 0.5 mL of fresh complete growth medium. The concentration of TRITC-Dextran in the abluminal medium was measured at 1, 2, and 4, and 24 h during reperfusion. A 50 µL of samples from the abluminal side were collected at indicated

time points. An equal volume of fresh medium was replaced to maintain the sink conditions. The concentration of TRITC-Dextran was measured using Synergy HTX multimode plate reader at excitation 485/20 and emission 580/50 nm. The diffusion rate of TRITC-Dextran at each time point was calculated as the amount of TRITC-Dextran present in the basolateral compartment per unit surface area of the insert per unit time.

$$Diffusion\ rate\ of\ TRITC-Dextran = \frac{Amount\ of\ TRITC-Dextran\ in\ basolateral\ compartment}{(Surface\ area\ of\ transwell\ insert)x(time\ at\ which\ basolateral\ sample\ was\ removed)} \quad \text{(Equation 2)}$$

2.15. Statistical analysis

Statistically significance among the mean of controls and treatment groups or within treatment groups were analyzed using one-way analysis of variance (ANOVA) or two-way ANOVA at 95% confidence intervals using GraphPad Prism 9 (GraphPad Software, LLC). The notations for the different levels of significance are indicated as follows: *p<0.05, **p<0.01, ***p<0.001, ****p<0.0001.

3. Results

3.1. EVs retained their physicochemical characteristics and membrane integrity upon revival from storage conditions. We collectively refer to sEV and m/lEV as EVs wherever applicable. We first studied the effect of storage conditions on the retention of physicochemical characteristics of hCMEC/D3-derived sEV and m/lEV using dynamic light scattering (**Fig. 1**). Freshly isolated sEV and m/lEV showed particle diameters of about 130 and 180 nm with

dispersity indices ranging from 0.35 to 0.4 (**Fig. 1 a-d**). There were no significant differences in the particle diameters of sEV between the fresh sample and after three freeze-thaw cycles (FT: samples were frozen at -20°C for 24 h and were thawed at room temperature for 30 min, **Fig. 1a**). Similar to sEV, m/lEV retained their particle diameters after three FT cycles with a consistent dispersity index (**Fig. 1b,d**). sEV and m/lEV showed an initial negative zeta potential of about -22 mV that ranged between -15 to -30 mV during three consecutive FT cycles (**Fig. 1e,f**). More than 90% of sEV and m/lEV (post-freeze-thaw cycles) showed a unimodal particle size distribution in the intensity plot (**Fig. S1**).

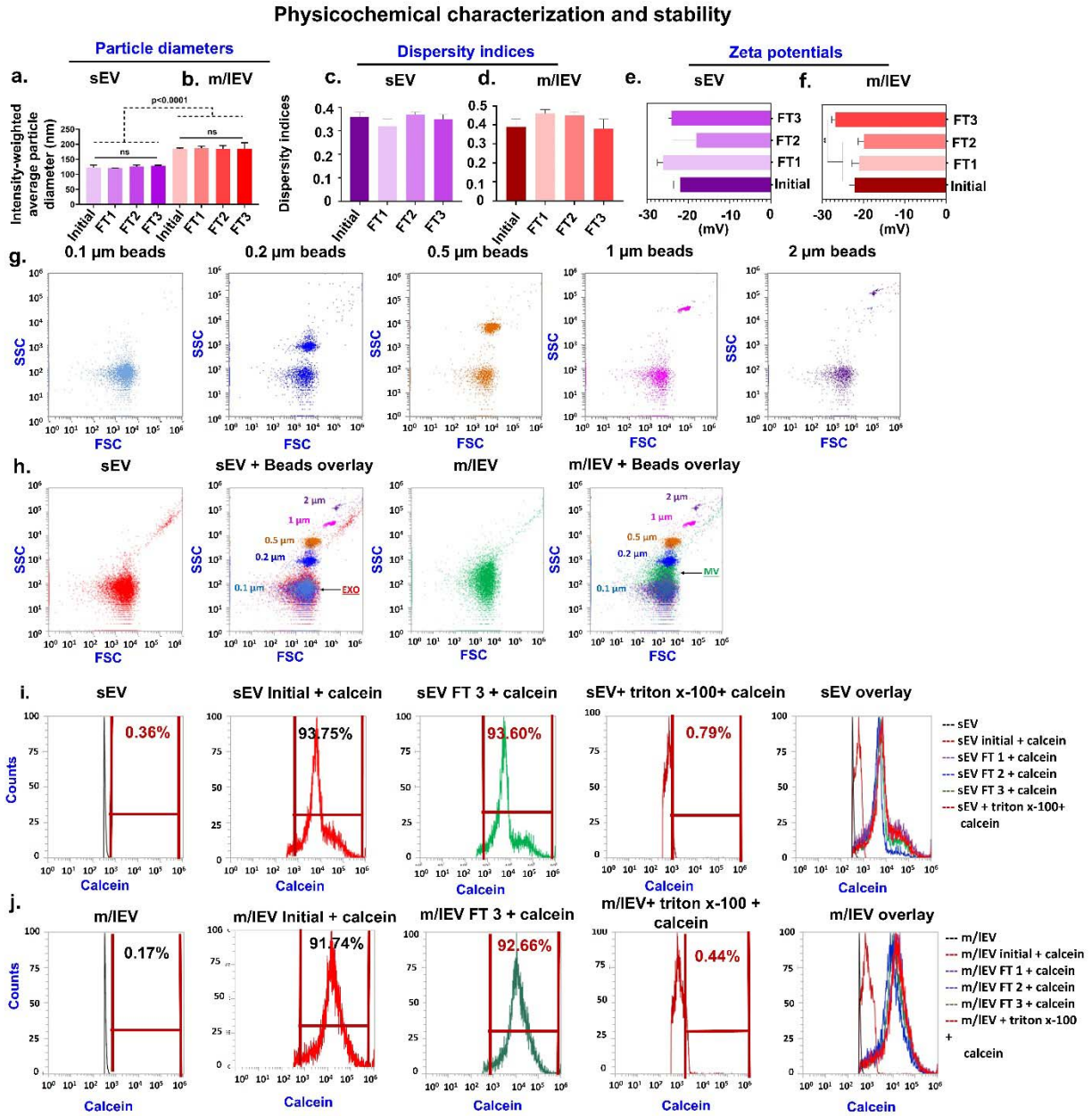

Fig. 1. Physicochemical characteristics and stability of EVs during storage conditions. Average particle diameters (**a,b**), and dispersity indices (**c,d**), and zeta potentials (**e,f**) of hCMEC/D3 cell line-derived EVs after three freeze-thaw (FT) cycles were determined using dynamic light scattering on a Malvern Zetasizer Pro-Red. Freshly-isolated samples (Initial) were used as controls. Samples were diluted to 0.5 mg protein/mL in 1x PBS for particle diameter and 10 mM HEPES buffer pH 7.4 for zeta potential measurements. The samples were stored at -20°C for 24 h and thawed at room temperature for 30 min prior to analysis. Data are presented as mean±SD of n=3 measurements. * $p<0.05$. The particle counts of polystyrene calibration beads, EXOs, and MVs were captured in forward scatter (FSC), side scatter (SSC) plots using Attune NxT flow cytometer (**g,h**). The histograms of calcein-positive events of intact EXOs (**i**) and MVs

(j) post-three FT cycles were detected using a small particle side scatter 488/10-nm filter in an Attune flow cytometer. Unstained EVs were used to gate the histograms for estimating percentage calcein-positive counts.

The membrane integrity of EVs during their storage conditions was determined using a previously reported calcein-based flow cytometry assay (29) that allows distinguishing the and histogram plots (**Fig. 1g-j**). Prior to analyzing the EVs, we first calibrated the flow cytometer using polystyrene beads of particle diameters ranging from 0.1 to 2 µm using a small particle side scatter filter (488/10 nm, BL1) (**Fig. 1g**). The relative position of EV clusters in the FSC/SSC overlay plots was directly proportional to the particle diameter since an increase in diameter showed a right-upward shift of the clusters. Notably, sEV and m/lEV clusters overlapped to a large extent in the area corresponding to 0.1-0.2 µm bead diameters suggesting that this flow cytometry method allowed us to detect EV-sized particles (**Fig. 1h**). The particle counts for PBS/calcein AM, unlabeled-sEV and m/lEV, PBS/Triton X-100/calcein AM mixture (sample processing controls) were acquired on SSC/BL1 density plots. Gates were created on the histogram and density plots to (1) distinguish the non-specific/background signals from PBS, calcein AM, and Triton X-100, and (2) measure the signal intensities of calcein-labeled EVs. About 90% of EXOs and MVs in freshly-isolated EV samples were calcein-positive suggesting that the EVs retained intact membranes after the ultracentrifugation and resuspension process (**Fig. 1i-j**). Importantly, >85-90% sEV and m/lEV remained their membrane integrity after three consecutive freeze-thaw cycles confirming the lack of significant membrane damage during and upon revival from storage conditions. In addition, EVs lysed with Triton X-100 showed less than 10% calcein-positive particle counts demonstrating the specificity of calcein signal intensities associated with the intact EVs.

We additionally performed an ATP assay to determine if EV retained their functionality upon revival from frozen storage conditions along with retention of their physicochemical characteristics. HBMECs under OGD conditions for 24 h showed about 60% reduction in relative ATP levels compared to normoxic HBMECs (**Fig. S2**). Importantly, HBMECs treated with freshly isolated sEV at 50 µg EV protein dose in OGD conditions showed about a three-fold ($p<0.0001$) increase in relative ATP levels compared to untreated cells (**Fig. S2**). OGD HBMECs treated with 50 µg sEV protein (sEVs were revived after three subsequent freeze/thaw cycles) showed a similar increase in relative ATP levels compared to untreated cells (**Fig. S2**). Importantly, there were no statistical ($p>0.05$) differences between relative ATP levels of HBMECs treated with either freshly isolated sEVs or sEVs post-freeze/thaw. Like sEV, OGD HBMECs treated with freshly isolated m/lEV showed about a four-fold and statistically significant ($p<0.0001$) increase in relative ATP levels compared to untreated cells (**Fig. S2**). Importantly, there was no statistical ($p>0.05$) difference between relative ATP levels of HBMECs treated with either freshly isolated m/lEV or freeze/thaw-subjected m/lEV. These observations suggest that EVs retain their functionality during frozen storage conditions.

3.2 m/lEV contain mitochondria and transfer their mitochondrial load to recipient primary HBMECs and hCMEC/D3 cells. We studied the morphology of naïve sEV and m/lEV isolated from hCMEC/D3 cells using transmission electron microscopy (TEM). TEM analysis of negatively-stained EVs showed nearly spherical sEV of about 50 nm (**Fig. 2a**) whereas m/lEV were ca. 200 nm structures (**Fig. 2b**). TEM images of sectioned sEV showed vesicles with particle diameters ranging from 20-100 nm and heterogeneous shapes (**Fig. 2c-e**). The core of

sEV appeared less dense and transparent suggesting that the core of sEV may not contain organelles like mitochondria and may instead contain cytosolic components.

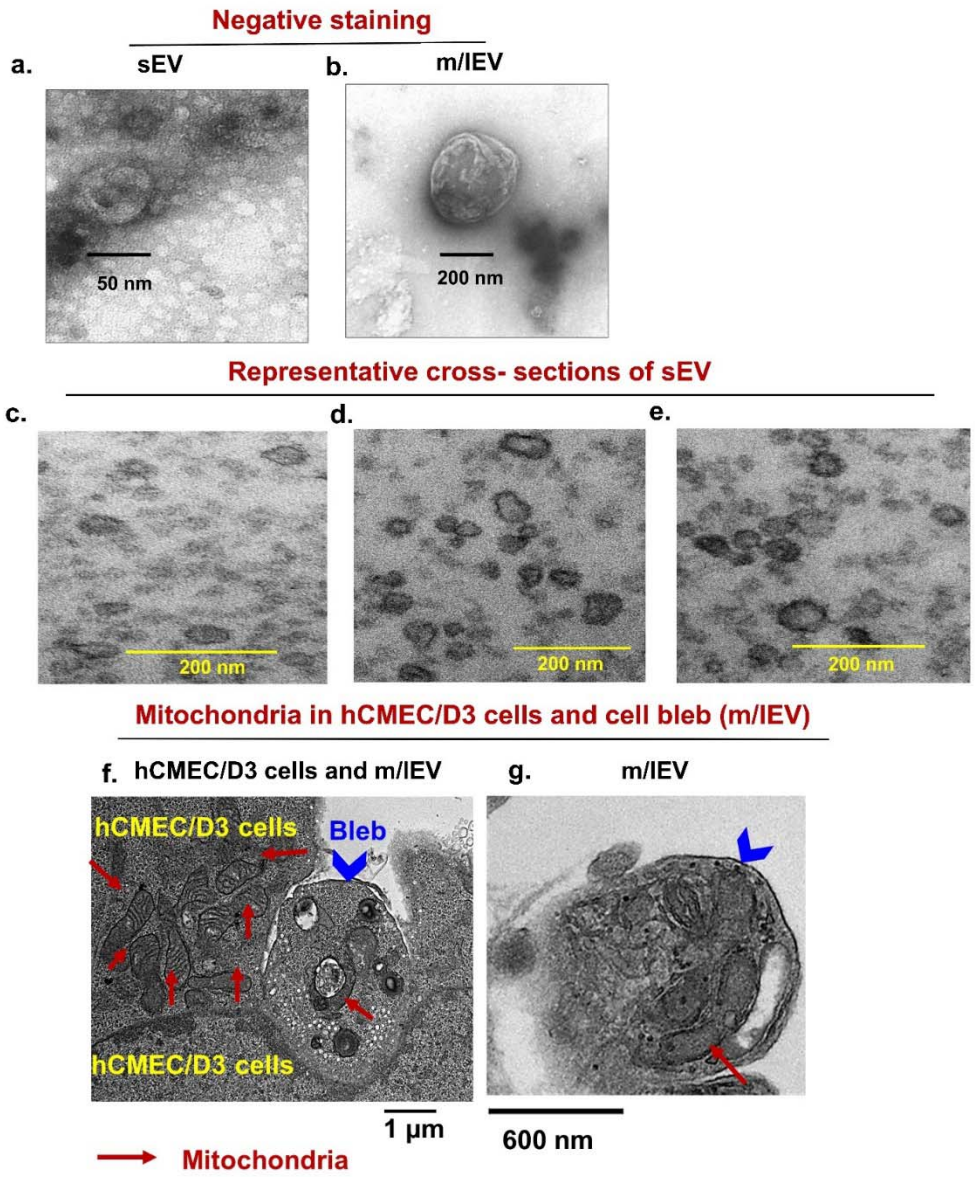

Fig 2. Transmission Electron Microscopy (TEM) analysis of EVs. (**a**,**b**) Negative stain TEM images of hCMEC/D3-derived sEV (**a**) and m/lEV (**b**). (**c-e**) TEM images of sectioned sEV. s (**f-h**). MVs show mitochondria. **(f-g)** hCMEC/D3 monolayers were cultured in a 6-well plate. The cells were washed with 1x PBS and fixed with 2.5% glutaraldehyde in PBS overnight. The cell suspension was pelleted, and ultrathin 70 nm sections were imaged using a JEOL JEM 1400 Plus transmission electron microscope. The blue arrowheads indicate hCMEC/D3 cell blebs (m/lEVs) containing mitochondria (maroon arrowheads).

We acquired TEM images of ultrathin, 70 nm sections of hCMEC/D3 cells (**Fig. 2f**) that also showed membrane blebs, suggestive of m/lEVs captured *in situ* (**Fig. 2f,g**). Small oblong to long, irregular tubular-shaped mitochondria was observed in hCMEC/D3 cells (maroon arrows**, Fig. 2f**). Importantly, hCMEC/D3-derived m/lEVs (blue arrowhead, **Fig. 2f,g**) showed the presence of mitochondria (maroon arrows) characterized by tubular or oblong-shaped structures with a characteristic double membrane. It should be noted that these in situ blebs were randomly captured during the plasma membrane budding. The bleb formation is consistent with m/lEV biogenesis that involves outward budding of vesicles from the cell's plasma membrane (5). It is important to note that hCMEC/D3 cellular mitochondria (**Fig. 2f**) were aligned near the plasma membrane and were eventually encapsulated into the m/lEVs. Interestingly, the observed m/lEV shapes was not spherical and relatively larger than known diameters of m/lEV: 100 - 1000 nm. The blebs may likely undergo further fragmentation/membrane rearrangement to produce mature m/lEVs. Our data (**Fig. 2f,g**) collectively demonstrate the presence of mitochondria in the m/lEVs.

Additional TEM images of cross-sectioned ml/EVs are also shown in **Fig. S3.** The blue arrow indicates the m/lEV membranes, whereas the maroon arrow points to mitochondria in m/lEV. Mitochondria were detected as structures with a characteristic double membrane. The high-speed centrifugation and extensive sample processing likely resulted in varying levels of recognition of double-membrane mitochondria. Notwithstanding, our data consistently showed that m/lEV- but not sEV sections contained mitochondria. Lastly, the observed morphology of mitochondria-rich EVs was consistent with published reports (6, 7).

Next, we wanted to determine if EVs can transfer their mitochondrial load into recipient HBMECs (**Fig 3a,b**). Therefore, we isolated sEV and m/lEV from hCMEC/D3 cells pre-stained with Mitotracker Red (MitoT-red). Donor hCMEC/D3 cells were treated with MitoT-red-sEV and MitoT-red-m/lEV at 30 to 150 µg EV protein/well for 72 h and MitoT-red signals in the recipient HBMECs were measured using flow cytometry. The intensity of MitoT-red-EVs in the recipient HBMECs (**Fig. 3a,b**) was analyzed using histogram plots. Untreated HBMECs cells were used as control and were gated for data analysis (**Fig. 3a,b**). Cells pre-stained with MitoT-red were used as a positive control and showed about 82% MitoT signals suggesting the presence of polarized mitochondria (**Fig. 3a,b**). Cells treated with unstained m/lEV did not show any MitoT-red signals in HBMECs suggesting the absence of non-specific MitoT signals (**Fig. 3a**). Cells treated with MitoT-red-m/lEV at a low dose of 10 µg dose showed about 32% MitoT-positive signals suggesting efficient mitochondrial transfer into the recipient HBMECs (**Fig. 3a,c)**. The fraction of cells showing Mito-T-+ve signals increased from 61% at 75 µg to 68% at 150 µg m/lEV dose (**Fig. 3a,c**). sEV at lower doses of 30 and 75 µg protein per well showed <5% of mitochondrial transfer which was increased to only about 13% at 150 µg dose (**Fig. 3b,c**). Cells treated with EV (sEV: m/lEV 1:1) at 75 µg EV protein showed about 54% MioT-red signal intensity suggesting that inclusion of m/lEVs in the EV mixture treatment increased mitochondrial transfer in HBMECs (**Fig. 3b,c**). As expected, m/lEV showed a greater transfer of mitochondria into recipient HBMECs compared to sEV consistent with the presence of notable mitochondrial load in m/lEV compared to sEV (**Fig. 2f-g, Fig. S3**).

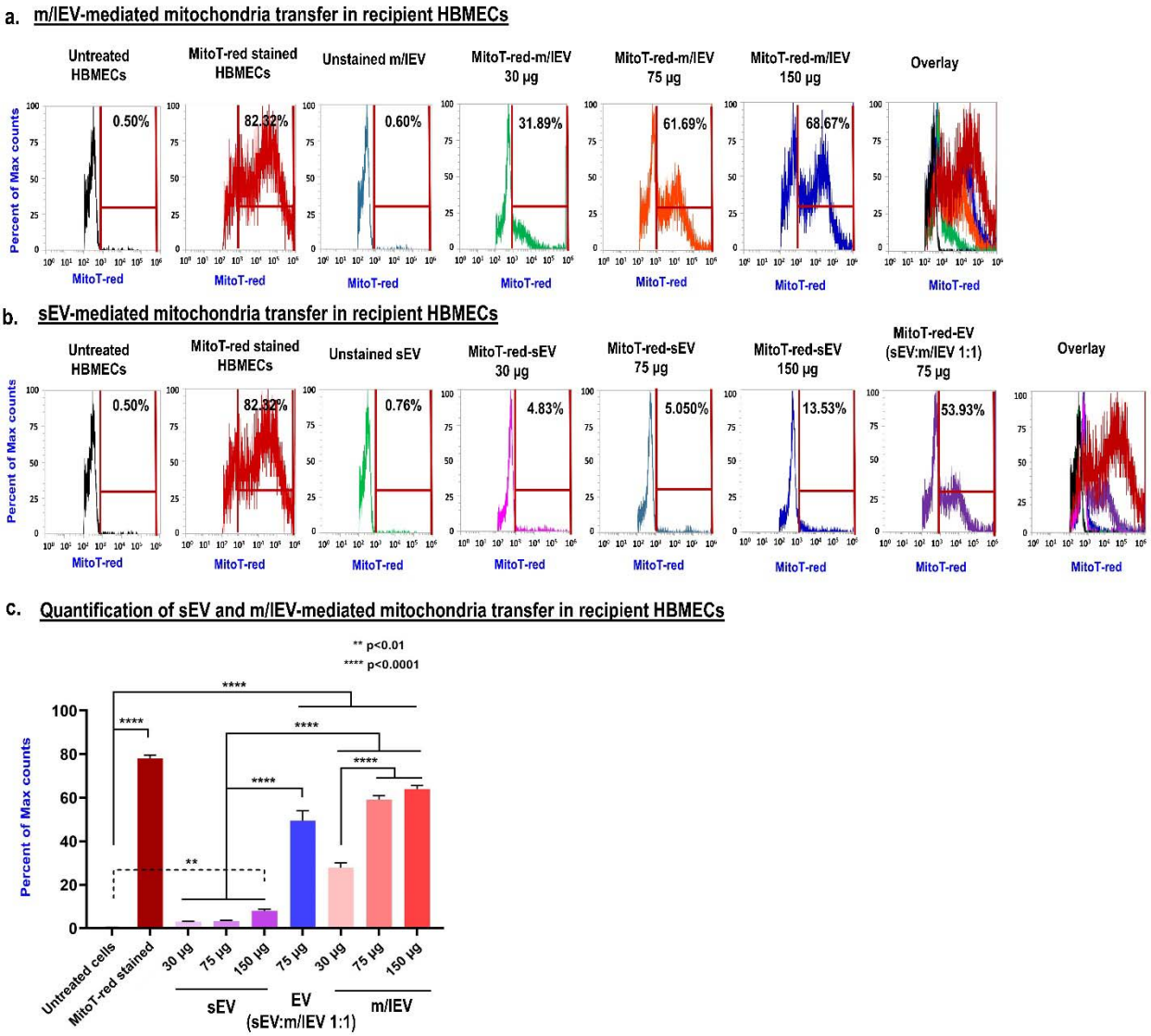

Fig. 3. Transfer of EV mitochondria into recipient HBMECs cells at varying doses. HBMECs cells were cultured in 48-well plates for 48 h in a humidified incubator. Cells were then incubated with the indicated amounts of MitoTracker red-labeled samples: (MitoT-red)-sEV, MitoT-red-EV (at a 1:1 sEV:m/lEV ratio, collectively referred to as EVs) and MitoT-red-m/lEV diluted in complete growth medium for 72 h. Post-incubation, the cells were washed, collected, and run through Attune NxT flow cytometer. The histograms of MitoT-red events of hCMEC/D3 cells treated at indicated doses of MitoT-red-MVs (**a**) and sEV (**b**) were detected using a 674/10-nm side scatter filter in an Attune flow cytometer. Unstained EVs were used to gate the histograms for estimating percentage MitoT-red-positive counts. (**c**) Quantification of sEV and m/lEV-mediated mitochondria transfer in recipient HBMECs. Data represent mean±SD of n=3.

We also studied EV-meditated mitochondrial transfer in recipient hCMEC/D3 cells (**Fig. S4**). Consistent with HBMECs, hCMEC/D3 cells treated with MitoT-red-m/lEV showed a dose-dependent increase in mitochondrial transfer from 48% at 30 µg to 68% at 150 µg dose (**Fig. S4a**). We noted a dose-dependent increase in the mitochondrial transfer that increased from 13% at 30 µg sEV to about 33% at the 150-µg dose (**Fig. S4b**). sEV-mediated mitochondrial transfer in hCMEC/D3 cells was comparatively greater than primary HBMECs (**Fig. 3b and Fig. S4b**).

3.3. EVs transferred polarized mitochondria to recipient primary human brain endothelial cells (HBMECs). EVs are known to contain functional mitochondria, mitochondrial proteins, and mtDNA along with their vesicular content of lipids, nucleic acid, and proteins (39, 40). We hypothesized that mitochondrial load in naïve EVs can be internalized into and subsequently integrate with the mitochondrial network of the recipient endothelial cells. We first determined the uptake of EV-associated mitochondria in recipient primary HBMECs and hCMEC/D3 cells. The recipient HBMECs or hCMEC/D3 cells were treated with Mitotracker red-stained EVs (MitoT-red-EV) for 72 h prior to observing under an epifluorescence microscope. Prior to evaluating the uptake of MitoT-red-EVs, we evaluated the cytocompatibility of hCMEC/D3 cells treated with MitoT-red-sEV and MitoT-red-m/lEV at different EV protein doses for 72 h and doses of 50 µg EV protein/well were well-tolerated by the cells (**Fig. S5**). No MitoT-red-associated signals were observed in unstained/untreated primary HBMECs suggesting that only MitoT-red specific signals were detected under the Cy5 channel (**Fig. 4a**). MitoT-red-sEV at 10 and 25 µg doses did not show positive signals in HBMECs for 48 h, however, MitoT-red-sEV at 50 µg doses showed faint intracellular Cy5 signals at 48 and 72 h suggesting low levels of mitochondrial uptake after 48 h (**Fig 4a**). In

contrast, strong intracellular signals in HBMECs treated with MitoT-sEV+m/lEV at the 25 µg (**Fig. 4a**) dose suggested that the inclusion of m/lEVs in the EV mixture led to an efficient uptake of polarized mitochondria into HBMECs. Moreover, the increase in sEV+m/lEV-mediated mitochondrial transfer was statistically significant ($p<0.01$) at 48 h compared to sEV alone (**Fig. 4b**).

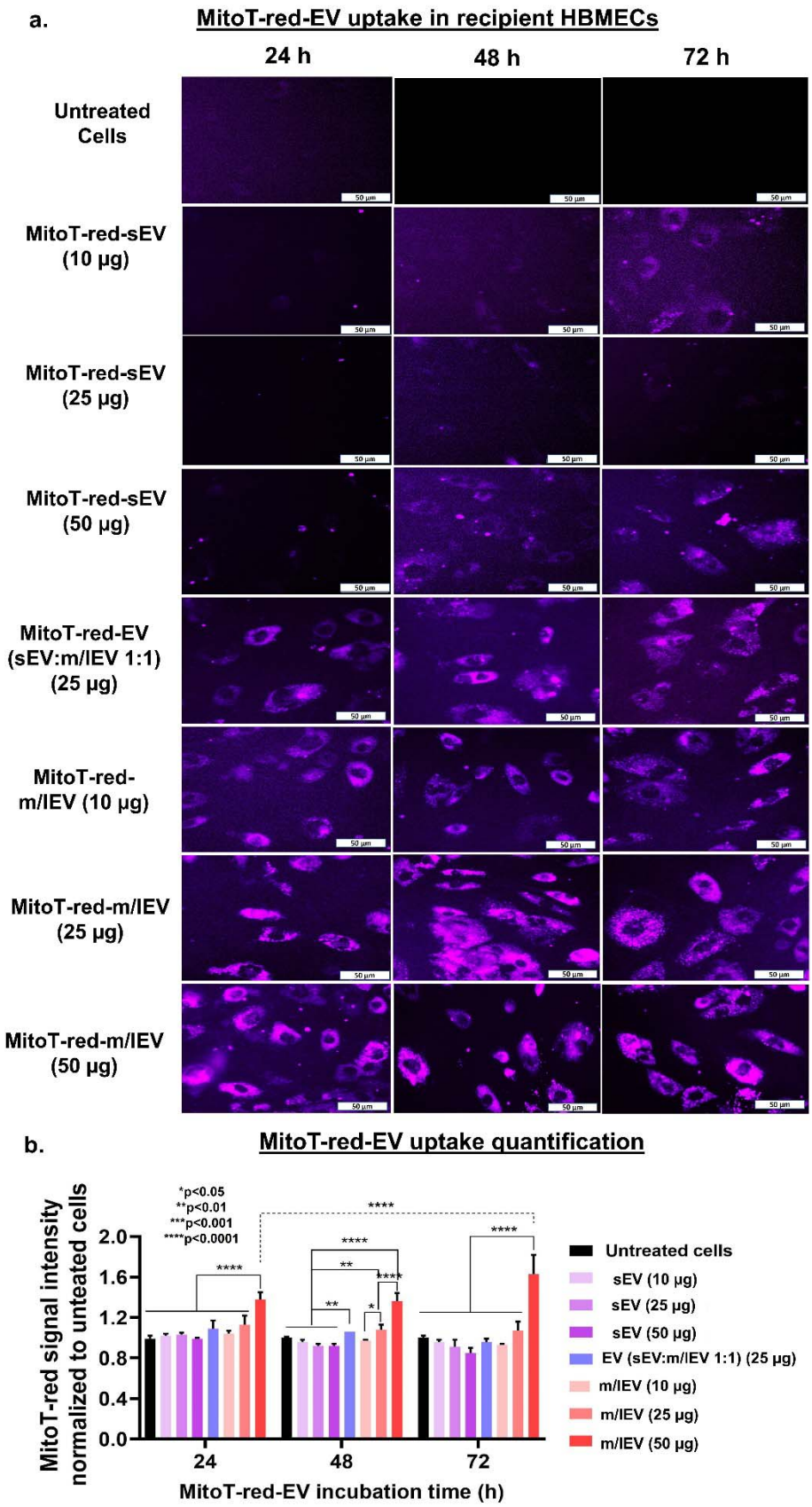
a.
MitoT-red-EV uptake in recipient HBMECs
24 h
48 h
72 h
Untreated Cells
MitoT-red-sEV (10 µg)
MitoT-red-sEV (25 µg)
MitoT-red-sEV (50 µg)
MitoT-red-EV (sEV:m/IEV 1:1) (25 µg)
MitoT-red-m/IEV (10 µg)
MitoT-red-m/IEV (25 µg)
MitoT-red-m/IEV (50 µg)
b.
MitoT-red-EV uptake quantification
*p<0.05
**p<0.01
***p<0.001
****p<0.0001
MitoT-red signal intensity normalized to unteated cells
MitoT-red-EV incubation time (h)
Untreated cells
sEV (10 µg)
sEV (25 µg)
sEV (50 µg)
EV (sEV:m/IEV 1:1) (25 µg)
m/IEV (10 µg)
m/IEV (25 µg)
m/IEV (50 µg)

706

Fig. 4. Transfer of EV mitochondrial load into the recipient HBMEC at varying doses and incubation times. (a) HBMECs were cultured in 96-well plates until 80% confluency in a humidified incubator. Cells were then incubated with the indicated amounts of MitoTracker red-labeled samples: (MitoT-red)-sEV, MitoT-red-EV (at a 1:1 sEV: m/lEV ratio), MitoT-red-MV diluted in complete growth medium for 24, 48, and 72 h. Post-incubation, the cells were washed and incubated with phenol-red-free growth medium. Intracellular MitoT-red-sEV/sEV:m/lEV/m/lEV signals were observed under an Olympus IX 73 epifluorescent inverted microscope using Cy5 channel (purple puncta) at 20x magnification. Scale bar: 50 µm. **(b) Quantification of MitoT-red-EV uptake**. HBMECs were treated with the indicated samples and doses for 24, 48, and 72 h. At each time point, from each control and treatment group, at least three images were acquired and the total sum of grayscale signal intensities in the Cy5 channel were estimated using Olympus CellSens software. The measured intensities were normalized with those of the untreated cells.

Interestingly, MitoT-red-m/lEV at a dose as low as 10 µg showed efficient uptake in HBMECs 72 h post-exposure. The levels of uptake increased significantly ($p<0.0001$) as the dose of MitoT-red-m/lEV increased from 10 to 50 µg at 48 h (**Fig. 4a,b**). The superior transfer of m/lEV-mediated mitochondria into HBMECs is likely due to a greater enrichment of functional mitochondria with a full complement of mitochondrial proteins in m/lEV compared to sEV. Therefore, it can be expected that m/lEV may increase the cellular bioenergetics of the recipient cells at lower doses compared to sEV. We further confirmed the effect of dose and type of EV subtype (m/lEV vs. sEV) on the transfer of mitochondria into hCMEC/D3 cells (**Fig. S6a**). Similar to the observations noted in the primary HBMEC cultures at 72 h post-exposure, sEV at 50 µg protein/well showed faint MitoT-red+ signals in the recipient hCMEC/D3 cells, whereas cells treated with MVs showed a dose-dependent increase ($p<0.01$) in mitochondrial transfer compared to sEV-treated endothelial cells (**Fig. S6a,b**).

We performed an additional experiment to compare the uptake of EVs stained with MitoT-red post-EV isolation vs. EVs that were isolated from donor cells prelabeled with MitoT-red. This study enabled us to evaluate if MitoTracker-labeled mitochondria proteins or fragments

may incorporate into sEVs and whether Mitrotracker can tag sEVs despite lacking whole mitochondria. Isolated EVs were incubated with MitoT-red to stain the polarized mitochondria, and the EV pellets were washed using 1*x* PBS to remove excess/free MitoT-red dye. Cells treated with sEV did not show any MitoT-red associated fluorescence in recipient HBMECs up to 25 µg EV protein dose but showed faint fluorescence at the 50 µg EV protein dose (**Fig. S7a**). MitoT-red-m/lEV showed a dose-dependent increase in MitoT-red fluorescent signals from 10 to 50 µg EV protein dose (**Fig. S7a**). Quantification of MitoT-red fluorescent signals (**Fig. S7b**) demonstrated a higher MitoT-red-mitochondria transfer from m/lEVs compared to sEVs irrespective of the EV-MitoT-red labeling method. EVs labeled post-isolation showed higher signal intensities than EVs isolated from pre-stained donor cells (**Fig. S7b**). The greater signal intensities may be related to the direct labeling of EVs with MitoT-red. In conclusion, we noted no significant differences in MitoT-red-EV uptake analyzed using EVs isolated from pre-stained donor cells vs. EVs stained post-isolation from donor cells. The greater extent of MitoT-red signals in m/lEV-treated recipient HBMEC suggests that m/lEV, but not sEV, contain functional mitochondria. In addition to staining polarized mitochondria, MitoT-red also covalently binds to cysteine thiols in mitochondrial inner membrane proteins (8). The weaker MitoT-red signals in sEV-treated recipient HBMECs likely indicate MitoT-red-stained mitochondrial proteins.

3.4. EV-transferred mitochondria colocalized with the mitochondrial network in the recipient endothelial cells

We wanted to determine if the EV-mediated transfer of mitochondria integrated with the mitochondrial of the recipient cells. We isolated MitoT-red-stained polarized mitochondria from the donor cells as we did earlier in section 3.3. and the recipient cell mitochondria were stained

using Mitotracker green (MitoT-green) and the overlap of these fluorescent signals was observed under an epifluorescent microscope. HBMECs and hCMEC/D3 cells pre-stained with Mitotracker green were incubated with MitoT-red-sEV and MitoT-red-m/lEV at 10, 25, and 50 µg doses for 72 h. Cytosolic, diffuse MitoT-green signals were observed under the GFP channel whereas punctate MitoT-red EV signals were captured under the Cy5 channel (purple puncta). The pre-staining of HBMECs with Mitotracker green resulted in robust fluorescent signals for 72 h and incubation with Mitrotracker red-stained EVs did not affect the Mitotracker green fluorescence intensities.

a. MitoT-red-EV colocalization with recipient HBMEC mitochondria

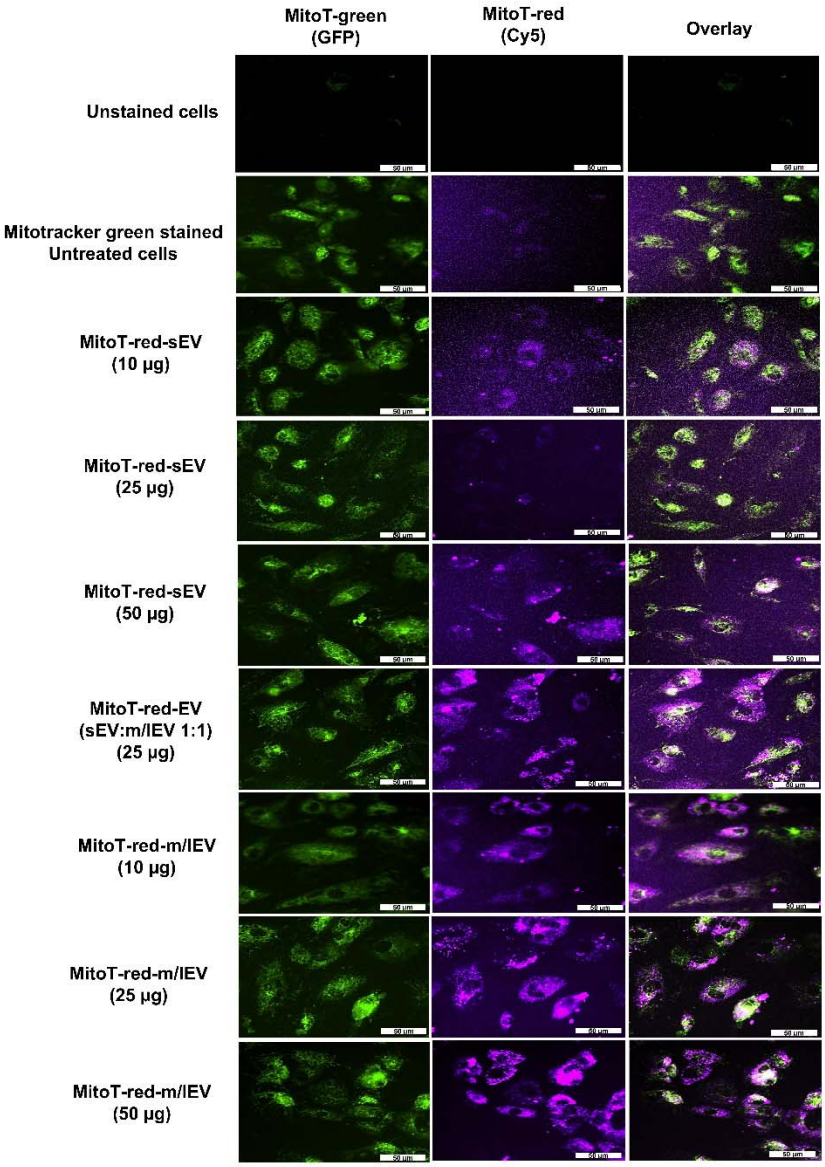

b. Quantitative analysis of MitoT-red-EV colocalization with recipient HBMEC mitochondria

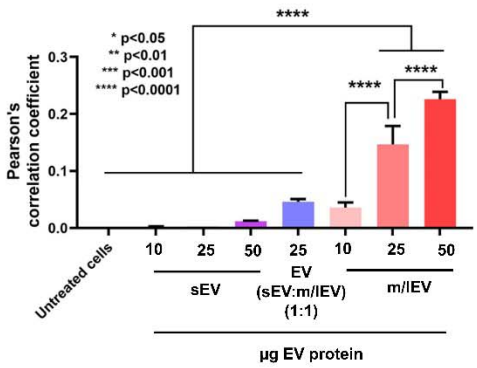

768

Fig. 5. Colocalization of EV mitochondrial load with the recipient HBMEC mitochondria. **(a)** HBMECs were cultured in 96-well plates until 80% confluency in a humidified incubator. HBMECs were stained with Mitotracker Green for 30 min. Post-staining, the cells were washed and treated with the indicated doses of MitoT-red-sEV, MitoT-red-EVs (at a 1:1 sEV: m/lEV ratio, collectively referred to as EVs), and MitoT-red-m/lEV for 72 h. Untreated cells and cells stained with MitoTracker Green only were used as controls. Post-incubation, the treatment mixture was replaced with phenol-red-free growth medium. The Mitotracker green staining in recipient HBMEC was acquired using the GFP channel, whereas the purple fluorescence associated with EV-transferred mitochondrial load was captured using Cy5 channel in an Olympus IX 73 epifluorescent inverted microscope. Colocalization of the mitochondrial signals was confirmed by the presence of yellow signals in the overlay images. Scale bar: 50 µm. (b) Pearson's correlation coefficient was obtained from the overlay images of Cy5 and GFP channels at constant signal intensities for both the channels using Cell Insight CX7 HCS microscope. Data are presented as mean±SD (n=3 images per treatment group). *p<0.05, **p<0.01, ***p<0.001, ****p<0.0001

The absence of GFP and Cy5 signals in untreated cells suggested the absence of non-specific signals at respective channel settings (**Fig. 5a**). The cells pre-stained with MitoT-green alone showed green cytosolic signals associated with recipient mitochondria (**Fig. 5a**). MitoT-red-m/lEV showed the greater intensity of Cy5 signals at all the tested doses compared to MitoT-red-sEV, once again demonstrating that m/lEV contain a greater mitochondrial load that efficiently integrate with the recipient cell's mitochondrial network compared to sEV (**Fig. 5a**). The overlay images of recipient HBMEC mitochondria and EV-associated polarized mitochondria in the m/lEV-treated cells showed considerably higher colocalization compared to sEV-treated cells (**Fig. 5a**). The Pearson's correlation coefficient (PCC) of GFP and Cy5 channel intensities demonstrated that sEV- and m/lEV- exposure resulted in a dose-dependent increase in colocalization (at least $p<0.05$), where m/lEV exposure showed statistically significant ($p<0.0001$) and a greater degree of mitochondria colocalization compared to sEV (**Fig. 5b**). Similar to the primary HBMEC cultures, hCMEC/D3 cells pre-stained with Mitotracker green

and treated with MitoT-red-m/lEV showed a greater degree of colocalization indicated by the overlap of MitoT-green and MitoT-red compared to sEV-treated cells (**Fig. S8**).

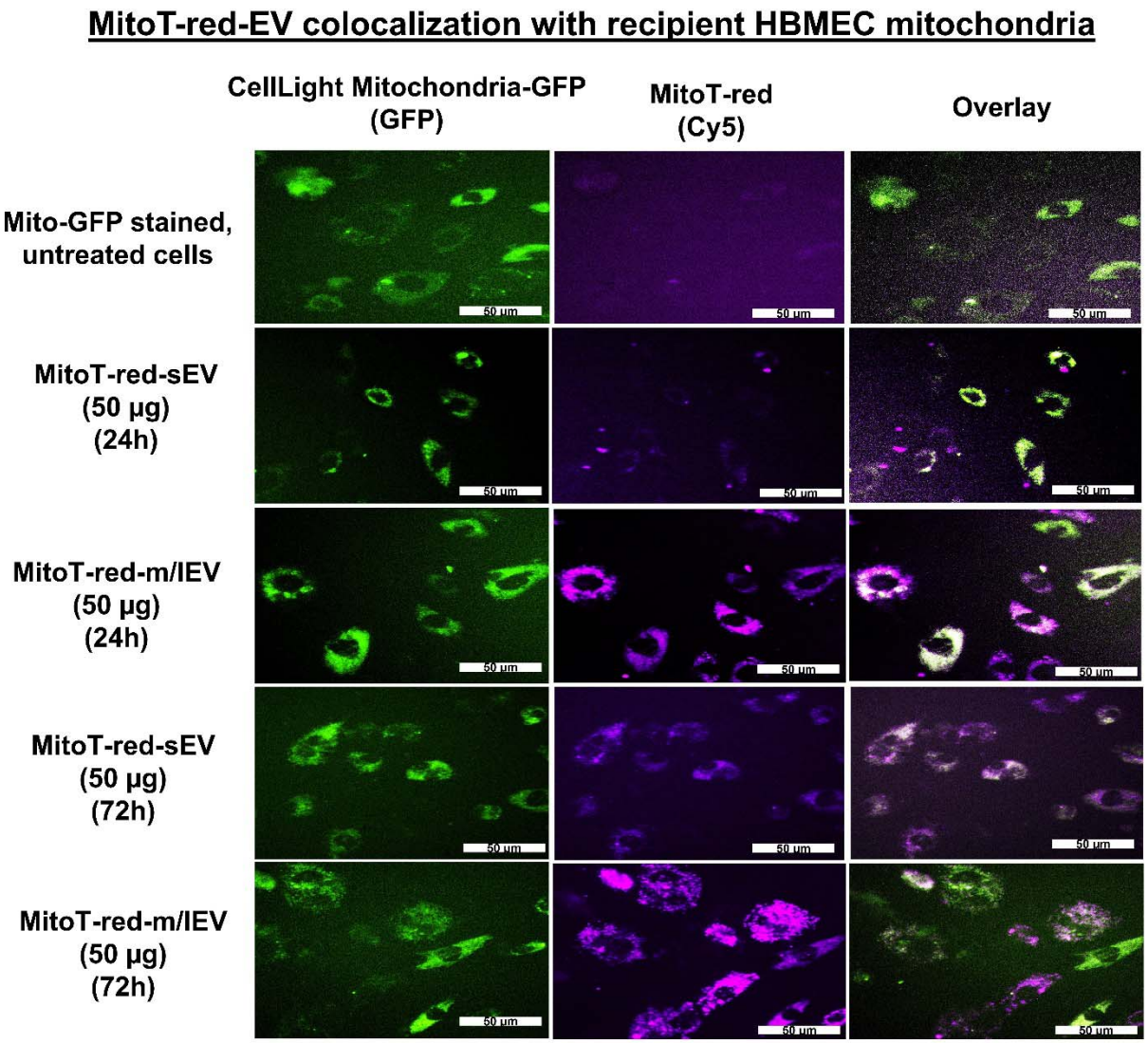

Fig. 6. Colocalization of EV mitochondrial load with the recipient HBMEC mitochondria using CellLight Mitochondria-GFP BacMam technique. (a) Confluent_HBMECs were transduced with CellLight Mitochondria-GFP at 2µL/10,000 cells for 16-18 h. The transduction mixture was then removed, cells were washed, and treated with a complete growth medium containing MitoT-red-EXO and MV at 50 µg/well for 24 and 72 h. Untreated cells and cells treated only with CellLight Mitochondria-GFP were used as controls. The green fluorescence associated with CellLight Mitochondria-GFP in recipient HBMECs was acquired using the GFP channel, whereas the purple fluorescence associated with polarized mitochondria from MitoT-

red sEV and m/lEV was captured using Cy5 channel using an Olympus IX 73 epifluorescent inverted microscope. Scale bar: 50 µm.

We further confirmed the integration of EV-mitochondrial components with mitochondria of the recipient cells using an orthogonal technique that allowed us to confirm that the EV-transferred mitochondria (functional, polarized mitochondria) integrated with the structural protein-stained mitochondria in the recipient cells. CellLight Mitochondria-GFP BacMam is a fusion construct of α-pyruvate dehydrogenase (a mitochondrial matrix protein) and emGFP packaged in a baculoviral vector that allows specific tagging of a structural mitochondrial protein (41). HBMECs and hCMEC/D3 cells were first transduced with CellLight Mitochondria-GFP (CellLight-MitoGFP) before MitoT-red-EV treatment. Despite the low absolute frequency of transduction (41), the recipient endothelial cells showed a strong GFP fluorescence suggesting that CellLight-MitoGFP transduction effectively tagged the alpha pyruvate structural mitochondrial protein in HBMECs (**Fig. 6**) and hCMEC/D3 (**Fig. S9**) cells. Similar to Figure 5, MitoT-red-m/lEV at a dose of 50 µg showed efficient transfer of mitochondria (purple puncta) in the recipient HBMECs and hCMEC/D3 cells. The EV MitoT-red puncta signals colocalized with recipient mitochondria (CellLight-MitoGFP) 72 h post-exposure. Notably, cells exposed to MitoT-red m/lEV showed greater Cy5 signals compared to MitoT-red-sEV-treated cells confirming again that m/lEV contain a greater level of mitochondrial load compared to sEV. The Cy5 signal intensity in m/lEV-treated cells was considerably increased at 72 h post-exposure compared to the 24 h time point suggesting that 72 h is an optimal exposure period for m/lEV internalization into the recipient HBMEC and hCMEC/D3 cultures (**Fig. 6 and S9**). Importantly, the overlap of the structural protein-tagged recipient cell mitochondria with the functional MitoT-red-stained m/lEV indicates that the m/lEV-delivered mitochondria colocalized with the

recipient cell mitochondria. In conclusion, our data collectively demonstrate that m/lEV contained a greater mitochondrial load compared to sEV and the m/lEV-associated mitochondria colocalized with the mitochondrial network in the recipient human brain endothelial cells. m/lEV-mediated mitochondrial transfer increased with increasing doses of m/lEV and the greatest colocalization with the recipient endothelial cells was observed at a 50-µg dose and 72 h incubation time.

3.5. Naïve EVs increased HBMEC ATP levels under normoxic and hypoxic conditions.

The effect of hCMEC/D3-derived EVs on the ATP levels in recipient primary HBMECs were evaluated under normoxic conditions using an ATP assay. Primary HBMEC monolayers were treated with sEV and m/lEV at 10, 25, and 50 µg EV protein per well for 24, 48, and 72 h. **Fig 7a** shows that the increase in HBMEC ATP levels upon sEV and m/lEV treatment for 24 h was not statistically significant ($p>0.05$). Importantly, HBMECs treated at a dose of 25 µg sEV for 48 h exposure showed a significant ($p<0.01$) increase in ATP levels compared to untreated cells. Interestingly, cells treated with m/lEV at 25 and 50 µg doses showed a dose-dependent and significant ($p<0.0001$) increase in relative ATP levels compared to untreated cells. In addition, the m/lEV-mediated increase in ATP levels was significantly ($p<0.05$) higher compared to sEV after 48 h exposure (**Fig. 7b**). At 72 h post-exposure, m/lEV at 25 and 50 µg doses showed a dose-dependent and significant ($p<0.01$) increase in relative ATP levels compared to untreated cells under normoxic conditions (**Fig. 7c**). In contrast, sEV did not show any significant increase in relative HBMEC ATP levels compared to the control. In addition, m/lEV-treated HBMECs showed significantly higher ATP levels compared to sEV at 72 h at all tested doses. The data suggested that the m/lEV-mediated significant increase in relative ATP levels at 48 h (**Fig. 7b**)

and 72 h (**Fig. 7c**) may likely be due to their inherent mitochondrial load—including mitochondria, mitochondrial DNA, and a full complement of mitochondrial proteins.

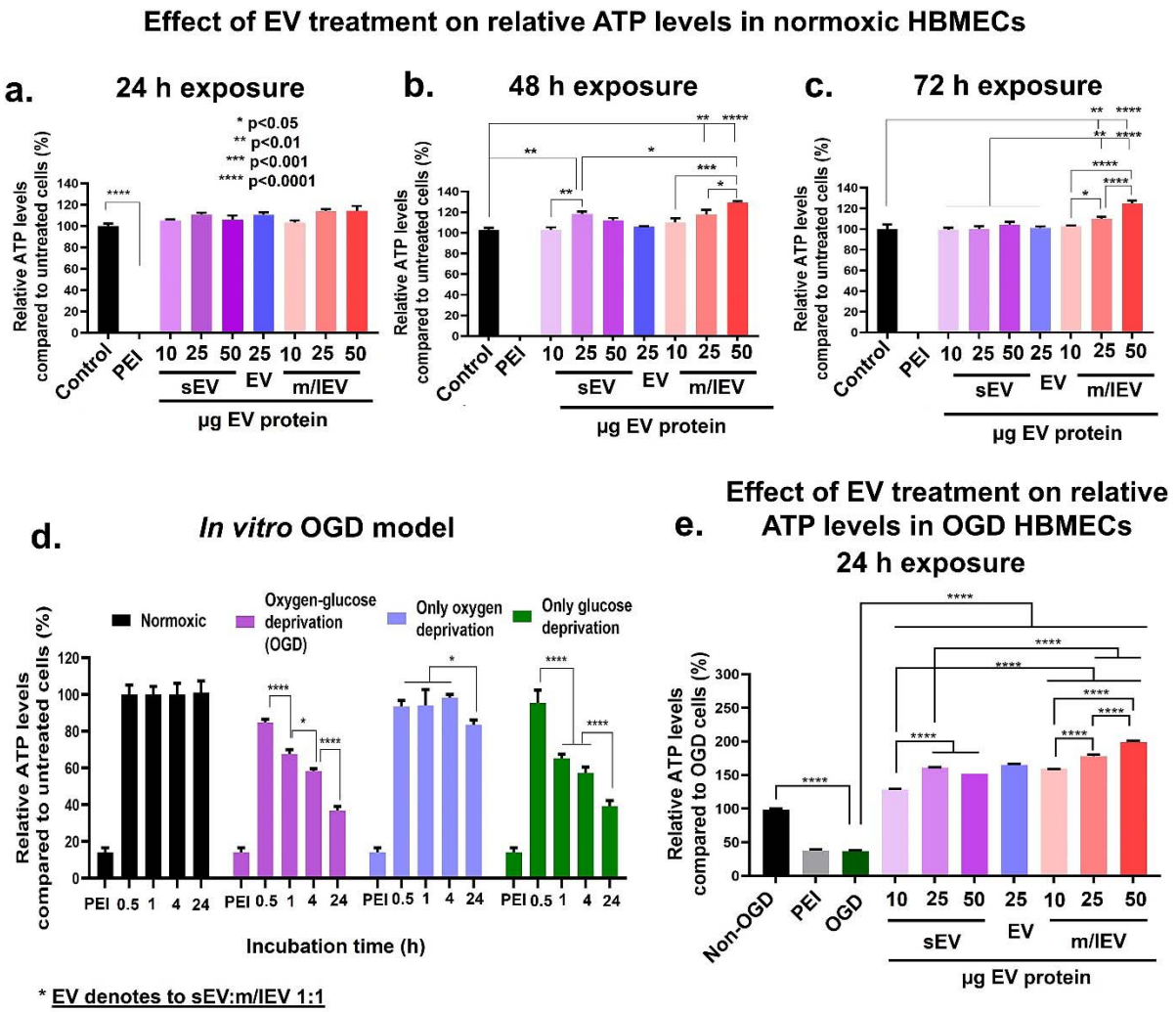

Fig. 7. EV-mediated increase in HBMEC ATP levels during normoxic and hypoxic conditions and cytocompatibility of polymer/HSP27 complexes with HBMEC. HBMEC cells were cultured in the 96-well plates until 80% confluency in a humidified incubator. (**a-c**) Confluent monolayers were treated with sEV, m/lEV, and EVs (sEV: m/lEV 1:1) at the indicated amounts for 24 (**a**), 48 (**b**), and 72h (**c**). Polyethyleneimine, PEI, at 50 µg/mL was used as a positive control for the ATP assay. Post-treatment, cells were incubated with a 1:1 mixture of fresh growth medium and Cell titer Glo reagent. The relative luminescence units (RLU) of the samples were measured using a SYNERGY HTX multimode plate reader at 1s integration time. Relative ATP levels were calculated by normalizing the RLU of treatment groups to the RLU of control, untreated cells. (**d**) Confluent normoxic HBMEC monolayers were treated with OGD medium and incubated in a hypoxic Billups-Rothenberg chamber at 37°C for 24 h. The following groups were also included: Normoxic HBMECs cultured in complete growth medium in a humidified incubator, oxygen-deprived cells cultured in complete growth medium in a

hypoxic chamber, glucose-deprived cells cultured in OGD medium in a normoxic chamber. The cell viability of normoxic HBMECs was used as a control to calculate the cell viability in all treatment conditions. (**e**) Confluent HBMECs were treated with the indicated doses of sEV and m/lEV in OGD medium and cell viability was measured 24 h post-treatment while untreated cells were used as a control. Data represent mean ±SD (n=3). * $p<0.05$, ** $p<0.01$, *** $p<0.001$, **** $p<0.0001$.

Ischemic conditions were simulated by culturing primary HBMECs under oxygen glucose-deprived (OGD), only oxygen-deprived, and only glucose-deprived conditions, and the resulting cell viability was evaluated from 0.5-24 h (**Fig. 7d**). HBMECs treated with complete growth medium and incubated in a humidified incubator (normoxic conditions) were used as a control for each time point. OGD HBMECs showed a time-dependent significant ($p<0.01$) decrease in cell viability compared to normoxic HBMECs. A four-hour OGD exposure led to about 40% cell death that further increased to about 60% at 24 h (**Fig. 7d**). Oxygen deprivation alone for 6 h did not result in a significant ($p>0.05$) decrease in cell viability, however, it caused nearly 20% cell death at 24 h. HBMEC cell viability decreased to about 60% during 2-6 h, followed by 50% cell viability at 24 h of glucose deprivation. To summarize, OGD-exposed HBMECs at 24 h showed a significant ($p<0.0001$) and maximum reduction in cell viability compared to other treatment conditions, therefore, we chose to expose HBMEC under OGD conditions for 24 h to simulate ischemic conditions for further experiments.

We studied whether naïve sEV and m/lEV can increase the cell survival of OGD-exposed primary HBMECs. HBMECs in OGD medium were incubated with sEV and m/lEV at 10, 25, and 50 µg EV protein/well for 24 h. The cell viability of EV-treated HBMEC cells was compared with untreated HBMECs maintained in OGD medium in a normoxic incubator (**Fig. 7e**). sEV and m/lEV at all treated doses showed a significant ($p<0.0001$) increase in cell viability

compared to control, untreated HBMECs (**Fig. 7e**). In addition, an increase in sEV and m/lEV dose from 10 to 25 µg EV protein/well showed a significant ($p<0.0001$) increase in ATP levels. HBMECs treated with m/lEV at 50 µg/well showed a maximum, ca. five-fold increase in ATP levels compared to untreated cells. Importantly, m/lEV showed a significantly ($p<0.0001$) higher HBMEC cell survival rate compared to sEV at the same dose (25 and 50 µg) suggesting that m/lEV outperformed sEV in increasing HBMEC cellular energetics under ischemic conditions. We also confirmed that the EV-mediated increase in endothelial cell viability under OGD conditions in the hCMEC/D3 cell line (**Fig. S10**). Consistent with primary human brain endothelial cells, hCMEC/D3 cells treated with EXOs and m/lEV at 10, 25, and 50 µg EV protein/well showed about a three to four-fold increase in endothelial ATP levels compared to ischemic cells under hypoxic conditions. Moreover, the EV-mediated increases in ischemic hCMEC/D3 cell survival were dose-dependent. Lastly, m/lEV-treated ischemic hCMEC/D3 cells showed a greater increase in ATP levels compared to EXO-treated cells (**Fig. S10**).

3.6. EVs increased the oxidative phosphorylation and glycolytic functions of recipient endothelial cells under normoxic and hypoxic conditions. The mitochondrial function of hCMEC/D3 cells treated with EVs under normoxic conditions was evaluated using Seahorse analysis by measuring oxygen consumption rate (OCR). hCMEC/D3 cells were treated with EXOs and MVs at 3.4, 8.3, and 16.5 µg protein/well in complete growth medium for 24, 48, and 72 h. The basal OCR, maximum OCR, and proton leak at each time point were measured for hCMEC/D3 cells treated with different doses of sEV and m/lEV. Basal and maximum OCR was not increased in sEV or m/lEV-treated cells compared to untreated cells at 24 and 48 h (**Fig. 8a,b**). In contrast, endothelial cells exposed to sEV and m/lEV for 72 h showed a dose-

dependent, significant ($p<0.0001$) increase in basal and maximum OCR compared to control, untreated cells, indicating that it takes 72 h for EV-mediated mitochondrial transfer and resulting increase in mitochondrial functions (**Fig. 7a-c and Fig. 4-6**). sEV at 16.5 µg protein/well showed a significant ($p<0.0001$) increase in OCR compared to 3.4 and 8.3 µg protein/well sEV doses. Besides, m/lEV at 3.4 µg protein/well showed a maximum and significant ($p<0.0001$) increase in OCR compared to higher m/lEV doses, and untreated cells. Importantly, m/lEV-mediated increase in OCR was significantly ($p<0.05$) higher compared to the maximum sEV dose suggesting that m/lEV outperformed sEV in increasing the recipient endothelial cells' mitochondrial function under normoxic conditions. The m/lEV-mediated increase in mitochondrial function was consistent with the m/lEV-mediated increase in cell viability in ATP assay (**Fig. 7**), intracellular uptake of m/lEV-associated mitochondria (**Fig. 4**), and the integration of m/lEV-associated mitochondria with the recipient cell's mitochondrial network (**Fig. 5, 6**). Notably, EV exposure did not affect proton leak for 72 h under normoxic conditions (**Fig. 8c**).

We further evaluated the effects of EVs on non-mitochondrial energy generation pathways such as cytosolic glycolytic capacity in the recipient endothelial cells. Extracellular acidification rate (ECAR) is a key indicator of cellular glycolysis and can be determined in real-time by measuring free protons in a Seahorse plate transient microchamber (42). ECAR (basal glycolysis rate and glycolytic capacity) was measured in hCMEC/D3 cells treated with sEV, m/lEV, and EVs (sEV+m/lEV at 1:1 w/w) at 3.4, 8.3, and 16.5 µg EV protein/well in complete growth medium (**Fig. 8d,e**). We did not note any changes in the basal glycolysis rate and glycolytic capacity of hCMEC/D3 cells pre-treated with sEV and m/lEV for 24 and 48 h compared to

untreated cells. However, treatment with 16.5 µg sEV for 72 h showed a significantly ($p<0.05$) greater basal glycolysis rate and glycolytic capacity compared to untreated cells. The glycolysis rate and glycolytic capacity of hCMEC/D3 cells were significantly ($p<0.01$) increased with an increase of sEV dose from 3.4 to 16.5 µg protein/well. Notably, sEV outperformed in increasing glycolysis capacity and basal glycolytic rate compared to m/lEV.

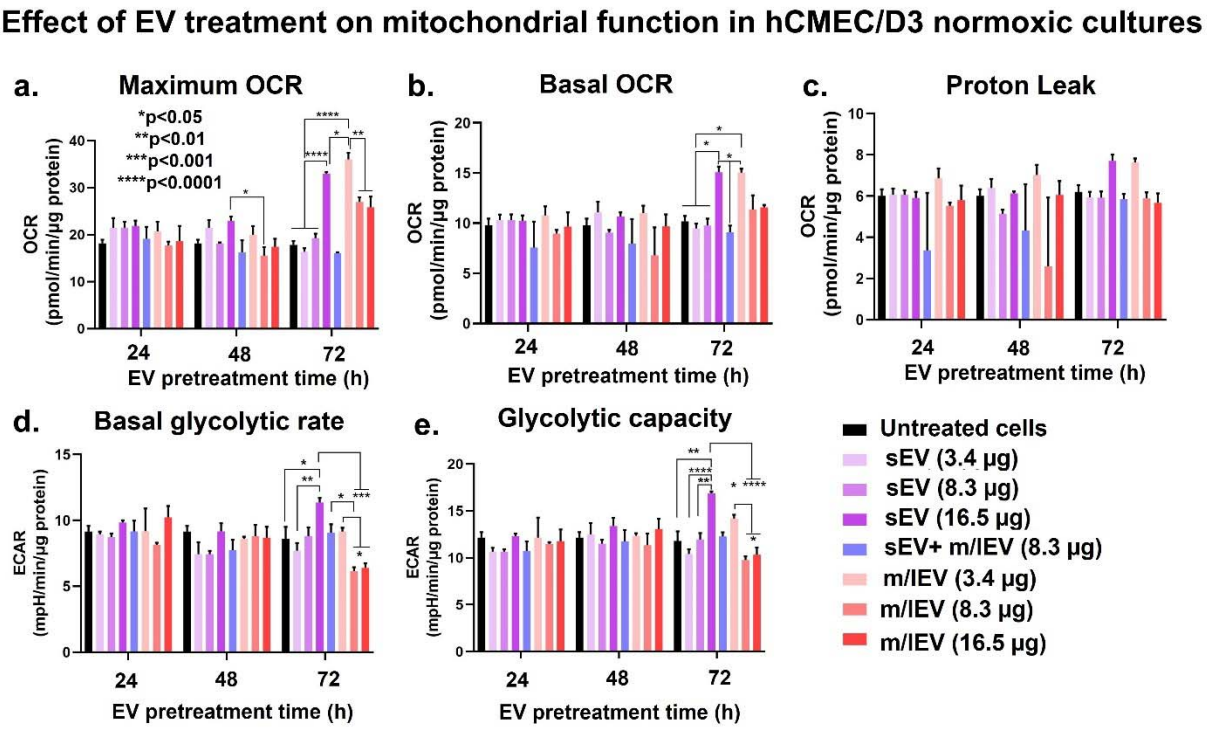

Fig. 8. Effects of EV exposure on mitochondria function in the recipient human brain endothelial cells under normoxic conditions. hCMEC/D3 cells were cultured in a Seahorse XF96 plate for 4 days at 20,000 cells/well. sEV, m/lEV, and EV (sEV+m/lEV; 1:1) were diluted in complete growth medium at the indicated doses of µg EV protein/well and cells were incubated in a humidified incubator for 24, 48, and 72 h. Post-treatment at each time point, the medium was replaced with DMEM and maximum oxygen consumption rate (OCR) (**a**), basal OCR (**b**), and proton leak (**c**) were measured using the Seahorse XFe96 analyzer. Basal glycolytic rate (**d**), and glycolytic capacity (**e**) were determined by measuring extracellular acidification rate (ECAR). Data represents mean±SEM (n=3). *$p<0.05$, **$p<0.01$, ***$p<0.001$, ****$p<0.0001$

The second goal of the present work was to evaluate the effects of HSP27 delivery on tracer permeability across the BBB in an OGD cell culture model of ischemia/reperfusion injury. We formulated EVs (a cell-derived, natural carrier) and a synthetic cationic polymer, PEG-DET, for the delivery of exogenous HSP27 protein. Followed by physicochemical characterization of the formed mixtures/complexes, we evaluated their effects on the paracellular permeability of small and large molecular mass fluorescent tracers across primary HBMEC monolayers exposed to OGD.

3.7. Exogenous HSP27 protein formed complexes with PEG-DET, EVs, and PEG-DET-EV mixtures. The complexation of HSP27 protein with PEG-DET and hCMEC/D3-derived EVs was determined by studying the electrophoretic mobility of HSP27 in a native polyacrylamide gel electrophoresis (PAGE) setup. Native recombinant human HSP27 at the running buffer of pH 8.3 carries a net negative charge (estimated charge: -4.2 mV) (43), and therefore, migrated from the loading spot towards the anode during electrophoresis (**Fig. 9a**). First, the complexation efficiency of PEG-DET with HSP27 was studied by comparing the relative changes in HSP27 band densities at polymer: protein weight/weight (w/w) ratios ranging from 0.05:1 to 20:1 (**Fig. 9a,b**). Compared to native HSP27 (100%, **Fig. 9b**), the relative band density of PEG-DET/HSP27 complexes at w/w 0.2:1 was considerably reduced to about 43%. As the w/w ratios increased, there was a gradual and significant decrease in HSP27 band densities (**Fig. 9a,b**). At PEG-DET/HSP27 w/w 10:1 and 20:1, the mean HSP27 band density decreased to nearly 25% suggesting that PEG-DET formed electrostatic complexes with HSP27 at physiological pH. The free polymer did not show any non-specific staining until the 1:1 w/w ratio. Non-specific

staining of free PEG-DET polymer was observed in the samples that contained an equivalent quantity polymer at w/w 5 and 10:1.

To determine if natural nanocarriers such as EVs can be formulated for the delivery of exogenous HSP27, hCMEC/D3 cell-line derived sEV and m/lEV were mixed with HSP27 at EV protein/HSP27 protein w/w ratios of 10:1 and the electrophoretic mobility of HSP27 was studied using native PAGE (**Fig. 9c-d)**. Mixtures of HSP27 with hCMEC/D3 cell line-derived sEV and m/lEV did not affect the migration of HSP27 at tested weight ratios (**Fig. 9c,**). The signal intensity of free/native HSP27 was set as 100%, and the relative band density of HSP27 in the different EV/HSP27 mixtures was compared with the band density of native HSP27. Though visually tricky to differentiate, the densitometry analysis showed that sEV/HSP27 and m/lEV/HSP27 mixtures decreased HSP27 band densities to about 77.5±20% and 84.1±2.4% compared to native HSP27 (100%), suggesting weak interactions between EV and HSP27 (**Fig. 9c-d, and Fig. S11a-d**). We do not consider this reduction in band intensity as HSP27 loading into EVs, but rather, we interpret this reduction to be a consequence of HSP27 and EV interactions.

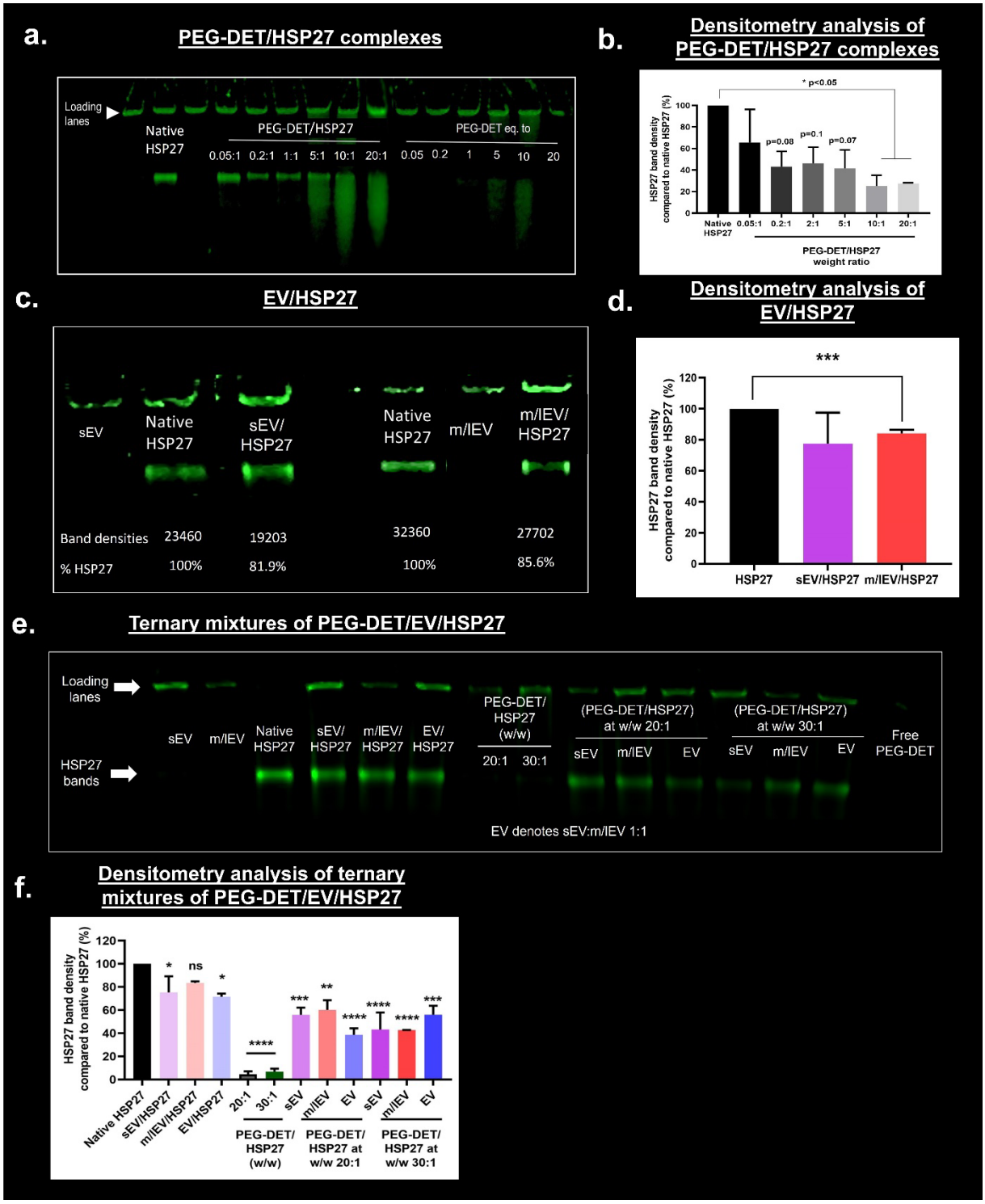

Fig. 9. Formation of EV- and PEG-DET/HSP27 complexes. (**a**) Native polyacrylamide gel electrophoresis (PAGE) for PEG-DET/HSP27 complexes. Native HSP27, PEG-DET/HSP27 at indicated weight ratios, and free PEG-DET polymers were mixed with 1x native sample buffer and loaded in an SDS-free 4-10% polyacrylamide gel at 1 µg HSP27 per lane. (**c**) Native PAGE for hCMEC/D3-derived EV/HSP27 complexes: Native HSP27 and mixtures of sEV/HSP27 , and

m/lEV/HSP27 at 10:1 weight/weight (w/w) ratios were loaded in a SDS-free 4-10% polyacrylamide gel at 1 µg HSP27 per lane. Free sEV and m/lEV equivalent to the amounts in 10:1 w/w complexes were used as controls. (**e**) Native PAGE for (PEG-DET/HSP27)/EV ternary mixtures. PEG-DET/HSP27 complexes were prepared at 20:1 and 30:1 w/w ratios followed by incubation with 10 µg of EVs. The indicated samples were loaded in the gel at 1 µg HSP27/lane. Each gel was run at 100 V for 2 h and stained using Biosafe Coomassie G250. The gel was then scanned at 800 nm using an Odyssey imager at intensity setting 5. (**b,d,f**) Densitometry analysis was performed by measuring band densities of HSP27 in the different experimental groups in comparison to the band density of native HSP27 in the respective gel using Image Studio 5.0 software *$p<0.05$

We then formulated ternary mixtures of PEG-DET/HSP27 complexes with hCMEC/D3-derived EVs, and the resulting changes in HSP27 band intensity were studied using native PAGE followed by densitometry analysis (**Fig. 9e,f**). sEV, m/lEV, and EV/HSP27 at w/w 10:1 showed about 20-40% reduction in band density whereas PEG-DET/HSP27 at w/w 20:1 and 30:1 showed >90% HSP27 complexation compared to native HSP27 (**Fig. 9f**). The HSP27 band density was decreased by 40-50% when PEG-DET/HSP27 at w/w 20:1 were incubated with 10 µg of sEV, m/lEV, and sEV+m/lEV 1:1 (EV). The % extent of reduction in HSP27 band density of (PEG-DET/HSP27)/EV complexes ranged among the values noted in the case of PEG-DET/HSP27 and EV/HSP27 complexes suggesting the competitive binding of negatively-charged EVs and HSP27 with the positively charged PEG-DET. Besides, increasing the relative amounts of PEG-DET in (PEG-DET/HSP27)/EV complexes further reduced HSP27 band density indicating the PEG-DET-mediated increase in complexation between HSP27 and EVs. To summarize, HSP27 formed electrostatic complexes with PEG-DET, non-ionic and weak interactions with hCMEC/D3-derived EVs, and ternary mixtures with both PEG-DET and HSP27: (PEG-DET/HSP27)/EVs.

3.8. Physicochemical characterization of the formed HSP27 complexes/mixtures

Particle diameters, dispersity indices, and zeta potentials of the formed complexes/mixtures were measured using dynamic light scattering (**Fig. 10**). The average diameter of native HSP27 protein was about 85 nm with a dispersity index of 0.27 (**Fig. 10a,b**). The average zeta potential of native HSP27 (1 µg/mL in 10 mM HEPES buffer, pH 7.4) was about -9 mV suggesting that HSP27 exerts net negative surface charge under physiological conditions (**Fig. 10c**).

The average particle diameter of PEG-DET/HSP27 complexes at 10:1 w/w ratio was over 1000 nm with a broad dispersity index. As the weight ratio increased from 20:1 to 30:1, the particle diameter significantly ($p<0.05$) decreased from about 359 nm to 205 nm with a very narrow dispersity index (**Fig. 10a,b**). PEG-DET/HSP27 complexes showed a unimodal particle size distribution in the intensity plots (**Fig. S12a**). PEG-DET/HSP27 complexes at 10:1 w/w ratio shifted the zeta potential of the native HSP27 protein from -9 mV to +10 mV confirming the electrostatic complexation of PEG-DET with HSP27. The zeta potentials, however, did not continue increasing for w/w ratios of 20:1 and 30:1.

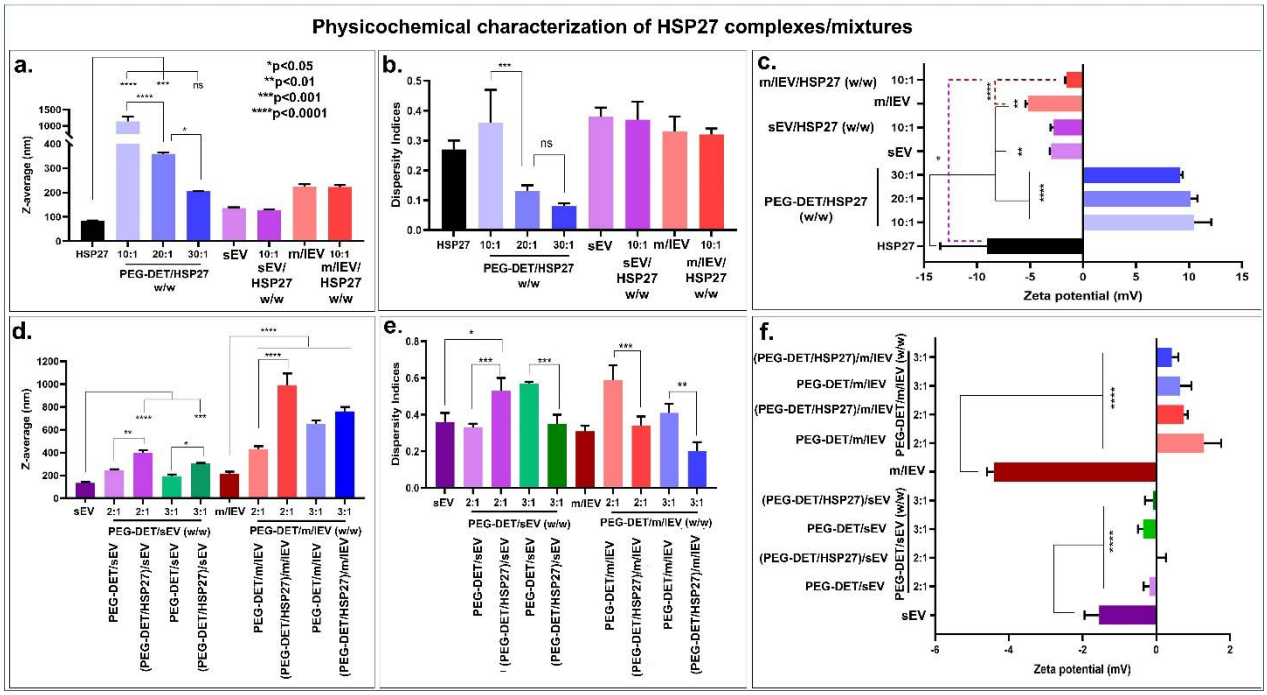

Fig. 10. Physicochemical characterization of HSP27 complexes with PEG-DET and EVs. Average particle diameters (**a**), dispersity indices (**b**), and zeta potentials (**c**) of the indicated samples were measured using dynamic light scattering on a Malvern Zetasizer Pro-Red. Average particle diameters (**d**), dispersity indices (**e**), and zeta potentials (**f**) of PEG-DET/EV and (PEG-DET/HSP27)/EV complexes at the indicated weight ratios. The samples containing 1 µg HSP27 protein were diluted to 50 µL in 10 mM HEPES buffer pH 7.4 for particle diameter measurements. The diluted samples were further diluted to 800 µL in 10 mM HEPES buffer pH 7.4 for zeta potential measurements. Data represent mean±SD (n=3). * $p<0.05$, ** $p<0.01$, *** $p<0.001$, **** $p<0.0001$

sEV and m/lEV derived from hCMEC/D3 cell lines showed diameters of about 136 and 225 nm respectively, with dispersity indices ranging from 0.3 to 0.4 (**Fig 10a,b**). sEV showed a bimodal particle size distribution compared to m/lEV (**Fig. S12c,e**). sEV/HSP27 or m/lEV/HSP27 mixtures at 10:1 w/w ratio did not change the average particle diameter and dispersity index compared to naïve EVs (**Fig. 10a,b**). In addition, the zeta potential of sEV and m/lEV were -3.01 and -5.20 mV respectively (**Fig. 10c** and **Fig. S12d,f**). The zeta potential of m/lEV/HSP27 mixtures shifted towards near-neutral values compared to naïve m/lEV and native HSP27 protein suggesting the formation of m/lEV/HSP27 complexes (**Fig. 10c**).

Next, PEG-DET was mixed with sEV and m/lEV at PEG-DET/EV w/w ratios 2:1 and 3:1, and the resulting changes in particle sizes, dispersity indices, and zeta potentials were compared with naïve sEV and m/lEV (**Fig. 10d-f**). The complexation of PEG-DET to sEV showed a considerable increase in particle size from 134 nm to 245 nm without affecting the dispersity index (**Fig. 10d,e**). The shift in mean zeta potential from -1.55 mV to -0.18 mV suggested the electrostatic interactions of PEG-DET and sEV (**Fig. 10f**). Furthermore, the z-average particle diameter of (PEG-DET/HSP27)/sEV significantly ($p<0.01$) increased to about 400 nm with a neutral zeta potential suggesting the interactions of PEG-DET/HSP27 and sEV (**Fig. 10d,f**). A similar trend was observed for m/lEV where the particle diameter was gradually and significantly ($p<0.0001$) increased from naïve m/lEV (216 nm), PEG-DET/m/lEV (431 nm), and (PEG-DET/HSP27)/m/lEV (991 nm) with dispersity indices ranging from 0.3-0.6 (**Fig. 10d,e**). A marked shift in zeta potential was observed from -4 mV for naïve m/lEV to 1.29 mV for PEG-DET/m/lEV, and 0.75 mV for (PEG-DET/HSP27)/m/lEV confirming the electrostatic interactions of PEG-DET and m/lEV (**Fig. 10f**). In addition, an increase in PEG-DET to EV w/w ratio from 2:1 to 3:1 showed a reduction in z-average diameter with a narrow dispersity index (**Fig 10d,e**). A slight decrease in zeta potential at PEG-DET/EV w/w 3:1 weight ratio suggested that increasing PEG-DET amount may increase the extent of complexation with EVs (**Fig. 10f**). The representative distribution plots of PEG-DET/EVs and (PEG-DET/HSP27)/EVs were shown in **Fig. S13**. To summarize, PEG-DET/HSP27 complexes showed a w/w ratio-dependent decrease in particle diameter with narrower dispersity indices and a positive surface charge. EV/HSP27 mixtures showed physicochemical characteristics more or less similar to naïve EVs.

The observed changes in particle diameter, dispersity index, and zeta potential of (PEG-DET/HSP27)/EVs confirmed the complexation of EVs with PEG-DET/HSP27 complexes.

3.9. PEG-DET/HSP27 complexes and EV/HSP27 mixtures were cytocompatible with primary human brain endothelial cells.

We performed an ATP assay on primary HBMECs treated with native HSP27, m/lEV, or sEV/HSP27 mixtures at w/w 10:1 and PEG-DET/HSP27 complexes at w/w 20:1 at a dose of 2 µg HSP27 per well. The cell viability of treatment groups was calculated using *Equation 1*. The average viability of cells treated with native HSP27 was 108.7% and there were no significant ($p>0.05$) differences between control, untreated cells, and native HSP27-treated groups suggesting that native HSP27 at 2 µg/well was well tolerated by HBMEC under normoxic conditions for 72 h (**Fig. S14a**). The cell viability of HBMECs increased significantly ($p<0.01$) when treated with sEV/HSP27 (124.7%), m/lEV/HSP27 (123.1%), and sEV+m/lEV /HSP27 (116.8) mixtures at 10:1 w/w ratio compared to untreated cells suggesting that EV/HSP27 mixtures were well tolerated by HBMEC for 72 h (**Fig. S14a**). The EV/HSP27 mixture-mediated increase in cell viability can be correlated with a significant increase in HBMEC ATP levels that was observed when cells were treated with naïve sEV (121%), m/lEV (126.4%), or sEV+m/lEV (120.1%) at amounts equivalent those present in the EV/HSP27 mixtures. HBMECs treated with PEG-DET/HSP27 complexes at w/w 20:1 treated showed an average 100.4% cell viability suggesting that PEG-DET/HSP27 complexes were cytocompatible for 72 h. Free PEG-DET polymer was also well tolerated by HBMECs for 72 h. Polyethyleneimine, a positive control, at 50 and 100 µg/mL concentrations showed a significant ($p<0.0001$) reduction in HBMEC viability indicating that the assay was responsive to the toxicities. We also confirmed the

cytocompatibility of HSP27 complexes with the hCMEC/D3 cell line (**Fig. S14b**). hCMEC/D3 monolayers treated with native HSP27, sEV or m/lEV/HSP27, and PEG-DET/HSP27 complexes treated showed >95% cell viability for 72 h demonstrating their cytocompatibility (**Fig. S14b**).

3.10. HSP27 complexes ameliorated the hypoxia-induced increase in BBB permeability in primary HBMECs

3.10.1. Paracellular permeability of 65-85 kD TRITC-Dextran (a large molecule tracer) in PEG-DET/HSP27 and EV/HSP27 pre-treated HBMECs. The effect of HSP27 complexed with PEG-DET and hCMEC/D3-derived EVs on the paracellular permeability of 65-85kD TRITC-Dextran was evaluated using primary HBMECs seeded in transwell cell culture inserts under normoxic and hypoxic/OGD conditions. The 65-85kD TRITC-Dextran was used a high molecular mass tracer simulating the diffusion of large molecules through the damaged BBB (9) and the effects of HSP27 delivery on decreasing the tracer diffusion rate. HBMECs were treated with HSP27 at a dose of 2 µg/well complexed with PEG-DET at 20:1 w/w ratio and sEV, m/lEV, EVs (sEV: m/lEV=1:1) at 10:1 w/w ratio. Native HSP27, free PEG-DET, and naïve sEV, m/lEV, and EVs were used as controls. Prior to subjecting cells to OGD (Pre-OGD) (**Fig. 11a**), cells treated with sEV/HSP27 mixtures showed a significant ($p<0.05$) reduction in TRITC-Dextran permeability compared to control, untreated cells. In addition, naïve sEV, m/lEV, and EVs showed a considerable decrease in 65-85 kD TRITC-Dextran permeability (**Fig. 11a**). The data suggested that naïve sEV and m/lEV and their HSP27 mixtures may increase the barrier properties of endothelial tight junctions compared to untreated cells under normoxic conditions.

Interestingly, cells treated with native HSP27 and PEG-DET/HSP27 complexes did not show any change in the TRITC-Dextran diffusion rate under normoxic conditions.

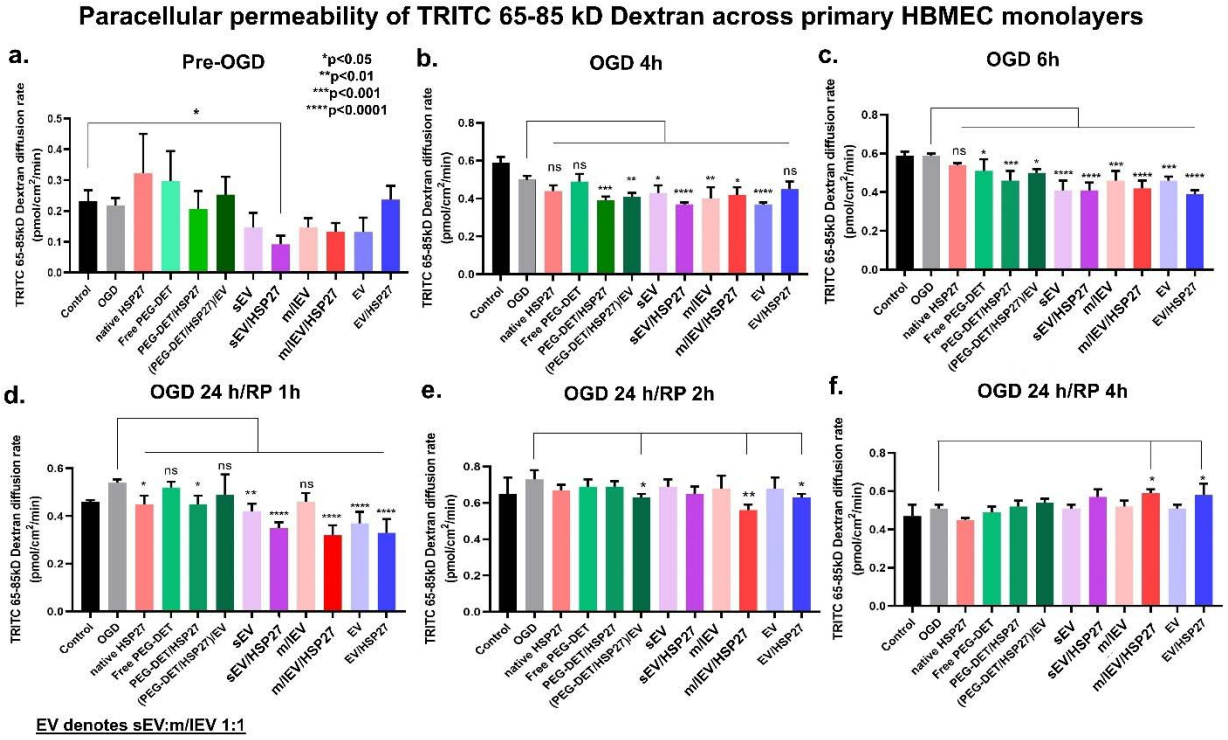

Fig. 11. Paracellular permeability of TRITC 65-85 kD Dextran under pre-OGD, OGD, and OGD/reperfusion conditions in HBMEC transwell culture inserts pre-treated with PEG-DET/HSP27 and EV/HSP27. HBMECs were seeded in 24-well plates and maintained in a 37°C humidified incubator for a week. The complete growth medium was replaced with 300 µL of growth media containing indicated treatment groups for 72 h. Post-incubation, the media was replaced with complete growth medium containing 1µM TRITC 65-85 kD Dextran for 1 h (Pre-OGD) **a**). Post-treatment, the treatment media was replaced with 300 µL of OGD medium containing 1 µM TRITC 65-85 kD Dextran for 24 h. The abluminal chamber was filled with 0.5 mL of complete growth medium. Control, untreated cells were incubated in complete growth medium in a humidified incubator whereas OGD treatment groups were incubated in an OGD chamber. At 4 (**b**) and 6 h post-OGD (**c**), a 500 µL volume was collected from the abluminal chamber and a fresh medium was added to the transwell inserts. Post-OGD treatment, HBMEC cells were washed with PBS and incubated with 300 µL of complete growth medium containing 1µM TRITC 65-85 kD Dextran and incubated in a humidified incubator for 1-24h. At each time point, a 500 µL volume was collected from the abluminal chamber and fresh medium was added to the transwell inserts. The concentration of TRITC 65 kD Dextran was measured at 1 h (OGD/RP 1h, **d**), 2 h (OGD/RP 2h, **e**), and 4 h (OGD/RP 4h, **f**) using a Synergy HTX multimode plate reader at 485/20 nm excitation and 580/50 nm emission settings. The diffusion rate of TRITC 65-85 kD Dextran at each time point was calculated by normalizing the amount of TRITC Dextran per unit surface area of the insert per unit time. Data represent mean±SD (n=2). * $p<0.05$, ** $p<0.01$, *** $p<0.001$, **** $p<0.0001$, ns: non-significant.

HBMECs pre-treated with PEG-DET/HSP27 complexes showed a significant ($p<0.001$) reduction in 65-85kD TRITC-Dextran diffusion during 4 h OGD exposure, whereas native HSP27 and free PEG-DET did not affect the permeability of high molecular weight dextran (**Fig. 11b**). sEV/HSP27 and m/lEV/HSP27 mixtures showed a significant ($p<0.0001$) reduction in 65-85 kD dextran diffusion rate compared to untreated OGD cells. Naïve sEV, m/lEV, and EVs also showed a statistically significant ($p<0.05$) reduction in dextran permeability under OGD conditions compared to untreated, OGD control (**Fig. 11b**). (PEG-DET/HSP27)/EV complexes also showed significant ($p<0.01$) reduction in 65-85 kD TRITC-Dextran diffusion rate compared to untreated cells at 4 h OGD. Exposure of cells to PEG-DET/HSP27, sEV/HSP27, m/lEV/HSP27, EV/HSP27, and (PEG-DET/HSP27)/EV complexes continued to decrease HBMEC permeability at 6 h OGD exposure showing a significant ($p<0.0001$) reduction in the 65-85 kD diffusion rate compared to the control (**Fig. 11c**). Importantly, naïve sEV, m/lEV, and EVs also showed a significant ($p<0.0001$) reduction in 65kD TRITC-Dextran paracellular diffusion rate compared to control (**Fig. 11c**). The data suggested that PEG-DET/HSP27 complexes can limit the diffusion of large molecules post-hypoxia/ischemia. Importantly, naive sEV and m/lEV limited the dextran diffusion before and during oxygen-glucose deprived conditions, whereas complexation of HSP27 with these EVs showed a synergistic effect on decreasing dextran diffusion during hypoxia/ischemia. Notably, there was no difference in the 65-85 kD TRITC-Dextran diffusion rate between control and HBMECs treated with HSP27 complexes at 24 h of OGD exposure (**Fig. S15a**).

Post-OGD, the OGD medium was replaced with fresh complete growth medium to evaluate the effect of HSP27 complexed with PEG-DET and EVs on the ischemia/reperfusion-mediated diffusion of 65kD TRITC-Dextran. Exposure of cells to PEG-DET/HSP27 complexes showed a significant ($p<0.05$) reduction in dextran diffusion rate 1 h post-ischemia/reperfusion (**Fig. 11d**). Importantly, sEV/HSP27, m/lEV/HSP27, and EV/HSP27 mixtures showed a significant ($p<0.0001$) reduction in dextran diffusion rate compared to OGD control after 1 h ischemia/reperfusion. Moreover, naïve sEV and EVs also showed significant ($p<0.05$) reduction in diffusion after reperfusion suggesting that naïve EVs increase brain endothelial tight junction integrity immediately after ischemia/reperfusion, and their mixtures with HSP27 synergistically reduce the large molecule infiltration across the brain endothelial cells (**Fig. 11d**). m/lEV/HSP27 and EV/HSP27 mixtures showed a significant ($p<0.05$) reduction in diffusion rate compared to OGD control 2 h post-ischemia/reperfusion, whereas the changes in the diffusion rate of dextran were insignificant ($p>0.05$) in other treatment groups compared to OGD control (**Fig. 11e**). It can be inferred that in addition to the naïve EV-mediated protection of BBB integrity pre-OGD/normoxia, during-OGD, and ischemia/reperfusion, their mixtures with HSP27 can provide prolonged endothelial protection during ischemia/reperfusion. There were no further differences in dextran diffusion rate amongst OGD control and treatment groups during 4-24h of ischemia/reperfusion (**Fig. 11f** and **S15b**).

3.10.2. Paracellular permeability of 4.4 kD TRITC-Dextran (a small molecule tracer) in PEG-DET/HSP27 and EV/HSP27 pre-treated HBMEC culture inserts

We measured the paracellular permeability of 4.4 kD TRITC-Dextran across HBMEC monolayers to evaluate the effect of PEG-DET/HSP27 and EV/HSP27 pre-treatment on the

paracellular permeability of small molecules in primary HBMECs during normoxic, ischemic, and ischemic/reperfusion conditions. HBMECs were treated at a dose of 2 μg/well HSP27 complexed with PEG-DET at 20:1 w/w ratio and sEV, m/lEV, EVs (sEV: m/lEV=1:1) at 10:1 w/w ratio. Native HSP27, free PEG-DET, and naïve sEV, m/lEV, and EVs were used as controls. The difference in the diffusion rate of 4.4 kD dextran between untreated and HSP27 complexes-treated cells during normoxic conditions and pre-OGD phase was not statistically significant ($p>0.05$) with the exceptions of MV/HSP27- and EV-treated groups (**Fig. 12a**). During the OGD phase, PEG-DET/HSP27, and (PEG-DET/HSP27)/EV-treated HBMECs showed a significant ($p<0.05$) reduction in the rates of 4.4 kD dextran diffusion compared to OGD, native HSP27, and free PEG-DET-treated HBMECs for 4 h (**Fig. 12b**). Besides, naïve sEV, m/lEV, and EV-treated HBMECs showed a significant ($p<0.05$) reduction in paracellular permeability for 4 h (**Fig. 12b**) and 6 h (**Fig. 12c**) of OGD exposure. Interestingly, HBMECs exposed to sEV/HSP27, m/lEV/HSP27, and EV/HSP27 did not affect the 4.4 kD dextran diffusion rate during 6 h of OGD. (PEG-DET/HSP27)/EV, naïve sEV, m/lEV, and EV/HSP27 mixtures showed a consistent and significant ($p<0.05$) reduction in the rate of 4.4 kD dextran diffusion for 24 h of OGD exposure (**Fig. S15c**).

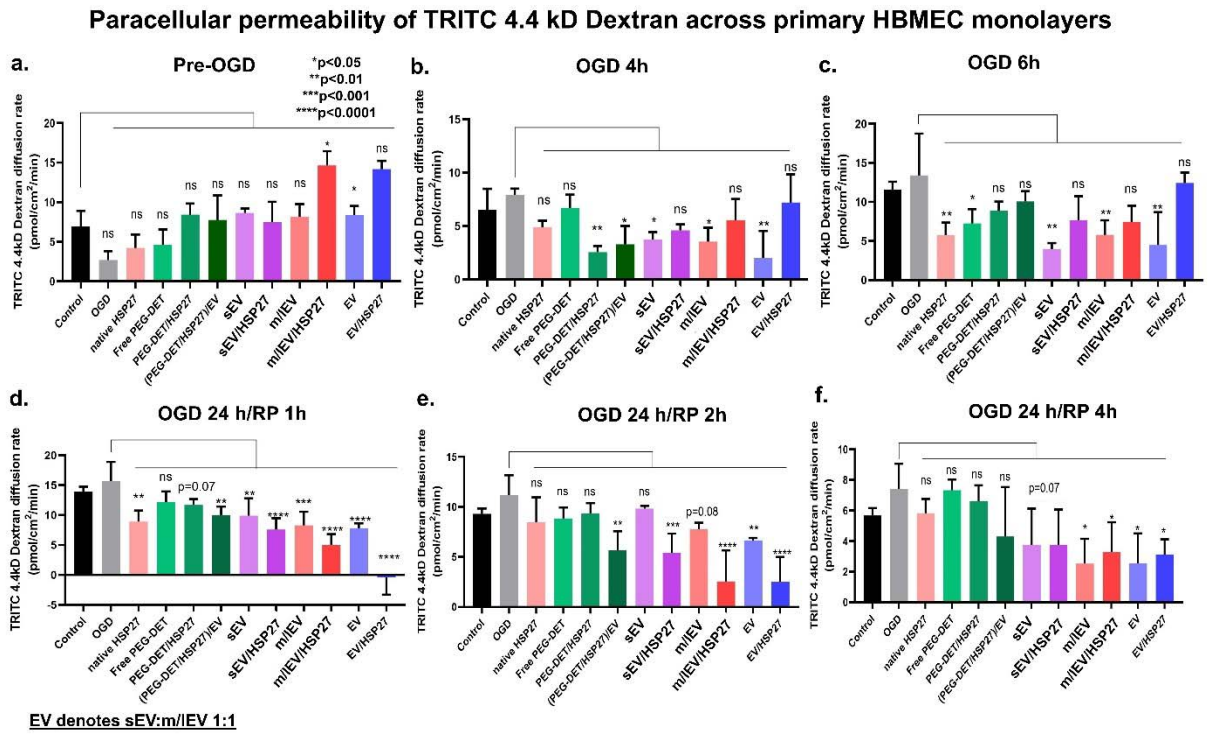

Fig. 12. Paracellular permeability of TRITC 4.4 kD Dextran under pre-OGD, OGD, and OGD/reperfusion conditions in HBMEC transwell culture inserts pre-treated with PEG-DET/HSP27 and EV/HSP27. HBMECs were seeded in 24-well plates and maintained in a 37°C humidified incubator for a week. The complete growth medium was replaced with 300 µL of growth media containing indicated treatment groups for 72 h. Post-incubation, the media was replaced with complete growth medium containing 1µM TRITC 4.4 kD Dextran for 1 h (Pre-OGD) **a**). Post-treatment, the treatment media was replaced with 300 µL of OGD medium containing 1 µM TRITC 4.4 kD Dextran for 24 h. The abluminal chamber was filled with 0.5 mL of complete growth medium. Control, untreated cells were incubated in complete growth medium in a humidified incubator whereas OGD treatment groups were incubated in an OGD chamber. At 4 (**b**) and 6 h post-OGD (**c**), a 500 µL volume was collected from the abluminal chamber and fresh medium was added to the transwell inserts. Post-OGD treatment, HBMECs were washed with PBS and incubated with 300 µL of complete growth medium containing 1µM TRITC 4.4 kD Dextran and incubated in a humidified incubator for 1-24h. At each time point, a 500 µL volume was collected from the abluminal chamber and fresh medium was added to the transwell inserts. The concentration of TRITC 4.4 kD Dextran was measured at 1 h (OGD/RP 1h, **d**), 2 h (OGD/RP 2h, **e**), and 4 h (OGD/RP 4h, **f**) using a Synergy HTX multimode plate reader at 485/20 nm excitation and 580/50 nm emission settings. The diffusion rate of TRITC 4.4 kD Dextran at each time point was calculated by normalizing the amount of TRITC Dextran per unit surface area of the insert per unit time. Data represent mean±SD (n=2). * $p<0.05$, ** $p<0.01$, *** $p<0.001$, **** $p<0.0001$, ns: non-significant.

During the first hour of ischemia/reperfusion (OGD/RP), HBMECs exposed to native HSP27 and PEG-DET/HSP27 complexes showed a significant ($p<0.05$) reduction in 4.4 kD dextran diffusion rate compared to OGD and free PEG-DET polymer-treated cells (**Fig. 12d**). In addition, naïve sEV, EVs, sEV/HSP27, m/lEV/HSP27, and EV/HSP27 pre-treated HBMECs showed a highly significant ($p<0.0001$) decrease in 4.4 kD dextran diffusion rate compared to control OGD/RP HBMECs (**Fig. 12d**). m/lEV/HSP27 and EV/HSP27-treatment mediated reduction in 4.4 kDa dextran diffusion rate was observed till 2 h of OGD/RP while the dextran diffusion rate in other treatment groups was non-significant compared to the untreated cells (**Fig. 12e**). There was no significant difference in dextran diffusion rate between control and treated OGD/RP HBMECs from 4 - 24 h (**Fig. 12f** and **S15d**). The possible reason for the observed lack of changes in the small molecule/4.4 kDa dextran diffusion rate during the reperfusion phase is likely due to the reperfusion-mediated rapid recovery of ischemic HBMECs.

4. Discussion

The lack of blood supply during ischemic stroke induces oxygen-glucose deprivation in brain tissues that results in sudden energy failure, mitochondrial damage, and disruption of tight junctions in brain endothelial cells lining the BBB (2, 4). The restoration of blood flow/"ischemia/reperfusion" further damages the BBB integrity leading to increased paracellular permeability of toxins and immune cells from blood to the brain parenchyma (7, 44-46). The damage to the BBB during ischemia/reperfusion disrupts the structure and function of the neurovascular unit and results in secondary brain damage leading to hemorrhagic transformation, poor neurological outcomes, and long-term cognitive impairment (9, 46). A treatment strategy that preserves the structure and function of the BBB would limit the infiltration of deleterious

molecules across the BBB, and consequently reduce the progression of brain injury and improve neurological functions in stroke patients (9). Therefore, a one-two-punch strategy to increase brain endothelial cell bioenergetics and decrease endothelial paracellular permeability is a promising approach to ameliorate ischemia/reperfusion-induced BBB damage post-ischemic stroke.

Endothelial overexpression of HSP27 in a transgenic mouse model of focal cerebral ischemia decreased mice brain infarct volume compared to neuronally-overexpressed HSP27 and placebo mice (9, 10, 47). Delivery of mitochondria is a novel approach to revive the bioenergetics of the damaged BBB. EVs are natural nanocarriers that are known to incorporate mitochondrial components such as mitochondria, mitochondrial DNA, and proteins along with their innate nucleic acid, lipids, and protein cargoes (40, 48-50). The goal of this study was to engineer EVs for the delivery of exogenous HSP27 protein along with the delivery of its innate mitochondrial load. The one-two-punch strategy is to harness the innate EV mitochondrial load to increase endothelial bioenergetics and deliver exogenous HSP27 protein to reduce paracellular permeability in ischemic endothelial cells. We believe that this approach to protect the brain endothelial cells is a potent strategy to decrease the long-term damage and dysfunction to the neurovascular unit. Protection of the neurovascular unit is increasingly recognized as a vital component (9, 10, 46) of novel stroke therapies.

The present study investigated (1) the naïve EV-mediated increase in mitochondrial function of recipient human brain endothelial cells under normoxic and ischemic conditions, and (2) the efficiency of EVs and a synthetic cationic polymer, PEG-DET, to deliver HSP27 and decrease

BBB permeability in ischemic brain endothelial cells. The results of our studies demonstrated that polarized mitochondria from EVs, specifically from m/lEV, were transferred into and colocalized with the mitochondrial network of the recipient endothelial cells. As a result, EV-treated primary HBMECs demonstrated increased intracellular ATP levels and mitochondrial respiration during normoxic and hypoxic conditions. EVs and PEG-DET polymer formed nano-sized complexes with recombinant human HSP27 protein. Importantly, prophylactic treatment of EV/HSP27 mixtures and PEG-DET/HSP27 complexes significantly reduced ischemia-induced paracellular permeability of small and large tracer molecules across primary HBMEC monolayers *in vitro*.

Brain endothelial cells form the foremost layer of the BBB and they contain about two to five-fold greater mitochondrial content compared to peripheral endothelial cells (51). Brain endothelial cell-derived EVs contain BBB receptors such as transferrin and insulin that enable EVs to cross the BBB for the treatment of various neurovascular disorders (52-54). A greater mitochondrial load and their natural affinity for BBB targeting motivated us to isolate sEV and m/lEV from a human cerebral microvascular endothelial (hCMEC/D3) cell line in our studies. We used a differential ultracentrifugation protocol, the most commonly used EV isolation method (55), to isolate m/lEV and sEV from the EV-conditioned medium. Post-ultracentrifugation and resuspension, sEV and m/lEV showed their characteristic particle diameters (100-250 nm, **Fig. 1a-d**) that largely aligned with the previous reports (19, 29, 39, 56, 57).

We have observed an apparent discrepancy between DLS and TEM sizing of sEVs and m/lEVs. TEM analysis of negatively stained EVs showed sEV of about 60 nm and m/lEV of about 250 nm diameter. In contrast, particle sizes of sEV and m/lEV measured by NTA/DLS was about 150 nm and 180 nm, respectively. For sEV, TEM analysis showed a smaller particle size than DLS measurements, whereas TEM sizing of m/lEV was higher than DLS. It is important to note that sEV and m/lEV are heterogenous EV subpopulations with polydispersity indices ranging from 0.3-0.4 (**Fig. 1c,d**). Therefore, the observed particle size differences of EVs measured by different techniques could be attributed to significant differences in the operating principles and sample handling/processing conditions. DLS and NTA estimate particle hydrodynamic diameters in a solvent. The hydrodynamic diameter includes the core of the particle and the surrounding liquid layer. On the other hand, TEM measures the core size of an individual particle in a dried state under vacuum. The environmental conditions may shrink the particles due to the osmotic diffusion of solvent from the aqueous core to the surrounding space. Importantly, TEM represents the morphology of only a small portion of the sample, which can further be affected by operator bias.

Anionic phospholipid components such as phosphatidylinositol, phosphatidylserine, and glycosylated lipid derivatives exert a net negative zeta potential on the sEV and m/lEV membranes (**Fig. 1e,f**) (50, 58). The broad polydispersity indices demonstrate the natural heterogeneity of both EV sub-populations. Similar to cells and other biomolecules, it is important to preserve EV physicochemical characteristics and biological activities during storage conditions which critically determine the scope of their therapeutic application. In our studies, sEV and m/lEV isolated from conditioned medium retained their particle diameters, dispersity

indices, and zeta potential after three consecutive freeze-thaw cycles (samples were frozen at -20°C for 24 h and then were thawed at room temperature for 1 h, **Fig. 1a-f**). Jeyaram *et al.* showed that EVs isolated from biofluids such as blood, milk, urine, and conditioned medium preserved their physical and functional properties stored at -80°C compared to 4° and -20°C (59, 60). Moreover, freeze-thaw cycles at -20° and -80°C did not affect the stability of plasma exosome miRNA (61). Lorincz *et al*. reported that 28 days of storage at -20° and -80°C did not affect the particle numbers of neutrophilic granulocyte-derived EVs, but moderately shifted their particle diameter and antibacterial activity (62).

The integrity of the sEV and m/lEV membranes immediately post-isolation and post-frozen storage were determined using a calcein-AM-based flow cytometry analysis. Calcein AM permeates the EV membranes, and as a result, intact vesicular esterases hydrolyze the acetoxymethyl-moiety of calcein AM to the non-permeant fluorescent calcein (63). The lack of esterases in damaged vesicles cannot activate the calcein-AM, therefore, this strategy can be utilized to differentiate intact vs. disrupted under a variety of conditions such as post- EV isolation, storage, freeze-thaw cycles, and at various osmolarities (63-65). Our analysis of calcein-labeled EVs indicated that freezing sEV and m/lEV at -20°C and thawing them thrice did not affect their particle count and membrane integrity compared to freshly-isolated EVs (**Fig. 1j,k**). Our results demonstrated that naïve sEV and m/lEV-isolated from conditioned medium preserved their physical characteristics, and at least >90% of EVs maintained their membrane integrity during the -20°C storage. Kong *et al.* utilized the calcein AM method to investigate the impact of storage conditions and anti-coagulants on m/lEV particle counts and sizes using flow cytometry (64). The authors reported that the particle counts of calcein-labeled MV significantly

decreased at -80°C storage for one to four weeks, however, remained unaffected during 4°C storage for a week. We performed an ATP assay to determine if EV retained their functionality upon revival from frozen storage conditions along with retention of their physicochemical characteristics. Our data showed that EVs retain their functionality during frozen storage conditions (**Fig. S2**)

We confirmed the presence of ATP5A protein (a subunit of mitochondrial adenosine triphosphate synthase complex (19, 66)) in m/lEVs using western blotting (**Fig. S16**) as we did in our previous studies (19, 29) , ATP5A plays important role in mitochondrial ATP production via catalyzing the synthesis of ATP from ADP in the mitochondrial matrix during oxidative phosphorylation (67). A considerably higher ATP5A band density in m/lEV compared to sEV suggested that MVs contain a greater mitochondrial load compared to sEV. Todkar *et al.* demonstrated that Optic Atrophy-1 and sorting nexin 9-dependent pathways play an important role in sorting mitochondrial proteins into EVs and prevented the incorporation of damage-associated molecular patterns into EVs (40). Phinney *et al.* have demonstrated that mesenchymal stem cells-derived MVs, but not EXOs, contained depolarized mitochondria (39). Mitochondria align with the plasma membranes and extrude into arrestin domain-containing protein-1-mediated m/lEVs as a pro-survival mechanism during physiological or oxidative stress-induced mitophagy (39). hCMEC/D3-derived sEV showed the presence of CD9 (**Fig. S16**), a tetraspanin sEV biomarker associated with exosomal cargo selection, binding, and uptake of sEV by target cells (68).We also noted the presence of CD9 in m/lEVs derived from hCMEC/D3 cells. Glyceraldehyde 3-phosphate dehydrogenase (GAPDH, 37 kD) was used as an additional marker to demonstrate the presence of cytosolic components in sEV and m/lEV (**Fig. S16**). We

performed western blotting in sEV and m/lEV lysates for determining the presence of TOMM20, outer mitochondrial membrane protein, as an additional mitochondrial marker (**Fig. S16b**). TOMM20, 16 kDa, is a translocase of the outer membrane receptor that regulates the import of specific proteins from the cytosol (20). The selective presence of TOMM20 in m/lEV and hCMEC/D3 cell lysates, but not in sEV lysates further confirmed that m/lEV contains mitochondrial proteins. Silva *et al*. also demonstrated the presence of TOMM20 in mesenchymal stromal cell-derived, mitochondria containing extracellular vesicles (21).

Mitochondria, the central metabolic hub of cells, are essential critical organelles especially in highly metabolic rate organs such as the brain (69). Cells cannot survive upon mitochondrial dysfunction-induced cellular energy deprivation. Therefore, mitochondrial replacement via supplementation of exogenous mitochondria or mitochondrial components is an efficient way to revitalize exhausted cells in many CNS disorders including ischemic stroke (72). Our TEM analysis demonstrated that m/lEV, but not sEV, showed the presence of mitochondria in m/lEV (**Fig. 2 f,g**). Mitochondria-rich MV structures was consistent with published reports (39, 73). Prior studies have demonstrated that mitochondria or mitochondrial components such as mtDNA, mitochondrial proteins were secreted into the extracellular milieu and transferred between CNS cells (39, 49, 74-78). For instance, mesenchymal stem cell-derived-MVs transferred mitochondria into the recipient macrophages leading to increased cellular bioenergetics (39). Guescini *et al.* demonstrated that exosomes were released from glioblastoma and astrocytes transfer mtDNA from glioblastoma to astrocytes (79).

We isolated sEV and m/lEV from the conditioned medium of Mitotracker deep red (MitoT-red) pre-stained hCMEC/D3 cells to label polarized mitochondria in EVs. MitoT-red is a mitochondrion membrane potential-dependent carbocyanine dye that selectively stains polarized mitochondria, and its fluorescence intensity is reduced during mitochondrial depolarization (80, 81). We demonstrated that m/lEV contain a greater polarized mitochondrial load compared to sEV and efficiently transfer mitochondria into recipient human brain endothelial cells (**Fig. 3a-c, 4 and Fig. S6**). m/lEV-associated mitochondria were transferred into the recipient endothelial cells within 24 h of incubation. Increasing the m/lEV dose and incubation time significantly increased mitochondrial transfer in the recipient cells. Importantly, the transferred mitochondria efficiently colocalized with the mitochondria network of recipient cells. The colocalization of EV mitochondria and recipient cell mitochondria was confirmed by the presence of overlapping signals of the EV-mitochondria fluorescence signals with the recipient mitochondrial signals. We used two orthogonal approaches to stain the mitochondrial network in the recipient cells: Mitotracker green and the CellLight mitochondria-GFP BacMam technique (**Fig. 5, 6 and Fig. S8, 9**). The carbocyanine Mitotracker green dye stains the functional mitochondria whereas CellLight Mitochondria-GFP BacMam comprising a fusion construct of α-pyruvate dehydrogenase and emGFP packaged in the baculoviral vector stains a structural mitochondrial matrix protein (α-pyruvate dehydrogenase) (41). Thus, utilizing two orthogonal types of staining techniques, we demonstrated an efficient colocalization of polarized EV mitochondria with the polarized mitochondria in the recipient cells (via Mito-T-green staining, **Fig. 5**) and integration of functional, polarized EV mitochondria with the structurally intact mitochondria in the recipient cells (via CellLight Mitochondria-GFP staining, **Fig. 6**). m/lEV and sEV showed a dose-dependent increase in colocalization at 72 h, specifically, the m/lEV mitochondria

demonstrated a significantly greater colocalization coefficient compared to sEV (**Fig. 5b**). The selective mitochondrial packaging into endothelial cell-derived m/lEVs compared to sEVs was consistent with published reports (39, 49, 79). Overall, our data demonstrated m/lEV-mediated transfer of functional mitochondria and their colocalization with recipient endothelial mitochondrial network.

One of the main functions of mitochondria is to synthesize ATP from ADP during mitochondrial aerobic respiration, and therefore, we measured the resulting relative ATP levels in the recipient endothelial cells treated with sEV or m/lEV using a Cell Glo ATP assay. Our results demonstrated that naïve sEV and m/lEV mediate a dose-dependent significant increase in the relative ATP levels at 48 h-post incubation (**Fig. 7a-c**). Importantly, m/lEV outperformed sEV in increasing recipient cell viability and the effects persisted for 72 h-post incubation (**Fig. 7b,c**). Islam *et al.* reported that mitochondria containing m/lEV derived from bone marrow stromal cells increased ATP levels of alveolar epithelial cells (75). Guo *et al*. demonstrated that transfer of mitochondria isolated from donor bone marrow-derived mesenchymal cells (BMSC) into the recipient BMSCs increased cellular ATP production, proliferation, migration, and repaired bone defects *in vitro* and *in vivo* (92).

Numerous studies have demonstrated the ischemia-induced cerebral endothelial dysfunction/apoptosis and BBB breakdown (93-96). In our studies, endothelial cells exposed to oxygen-glucose deprived (OGD) exposure in a hypoxic chamber led to about 40% and 60% endothelial cell death at 4 and 24 h, respectively, compared to untreated cells (**Fig. 7d**). The observed data is consistent with the published reports (97, 98). Our results showed that primary

HBMECs treated with hCMEC/D3-derived naïve sEV and m/lEV resulted in a four to five-fold increase in endothelial ATP levels compared to control, untreated cells (**Fig. 7e**). Importantly, EV-mediated increases in ATP levels were dose-dependent and m/lEV outperformed compared to sEV in rescuing the ATP levels and consequently the survival of ischemic HBMECs 24 h post-OGD (**Fig. 7e**). Our western blot (**Fig. S16**) and published reports (39, 40) suggest that the m/lEV-mediated increase in recipient endothelial cell ATP levels is associated with the presence of functional mitochondria and mitochondrial proteins. High throughput proteomic analysis revealed 89 types of mitochondrial proteins in m/lEV vs. a single type in sEV isolated from hCMEC/D3 cells (33). The presence of mitochondrial components such as mtDNA and mitochondrial proteins in sEV can also enhance cellular mitochondrial function (33, 56). sEV isolated from healthy and asthmatic human airway myeloid-derived regulatory cells incorporated mitochondria that subsequently transferred and colocalized with the mitochondria of recipient T cells (33). Kong *et al.* reported that treatment with mesenchymal stem cell (MSC)-derived exosomes rescued OGD-induced rat primary brain endothelial cell death (99). Arslan *et al.* reported that MSC-derived exosomes resulted in a two-fold increase in ATP levels in ischemia/reperfused mice compared to saline control (100). The authors reported that administration of sEV five minutes prior to reperfusion in ischemic mice showed about a 45% decrease in mice myocardium infarct volume compared to saline treatment. Besides, D'Acunzo *et al*. identified a novel population of EVs, "mitovesicles" derived from mitochondrial membranes but do not contain mitochondria. The authors showed that mitovesicles were metabolically active, and murine hemibrain-isolated mitovesicles showed a two-fold increase in brain ATP levels compared to oligomycin and antimycin-I treated EVs. (101). Overall, m/lEV-associated mitochondria and exosomal mtDNA and/or mitochondrial proteins have shown the potential to

rescue normoxic and ischemic endothelial cells in a dose- and time-dependent manner by increasing intracellular ATP levels.

Metabolic pathways such as mitochondrial respiration and glycolysis are the major sources of ATP for cellular energy production (102). Therefore, we investigated the effects of m/lEV and sEV treatment on mitochondrial respiration and glycolytic capacity function in the recipient endothelial cells using a Seahorse setup. The state-of-art Seahorse extracellular flux (XF) analyzer allows real-time analysis of extracellular acidification rate (ECAR), an indicator of glycolysis, and the oxygen consumption rates (OCR), an indicator of mitochondrial respiration in live intact cells (103, 104).

We demonstrated that hCMEC/D3 cells treated with sEV and m/lEV show a dose-dependent significant increase in basal and maximum OCR at 72 h exposure (**Fig. 8a-c**). Consistent with ATP assays (**Fig. 7a-c**), the m/lEV-mediated increase in maximum mitochondrial respiration was greater than sEV suggesting that m/lEV mitochondria efficiently increased the recipient cell mitochondrial function under physiological/normoxic conditions. Interestingly, we noted that sEV showed a dose-dependent and significantly greater increase in recipient glycolysis capacity compared to m/lEV. We speculate that m/lEV likely colocalize with the mitochondria whereas sEV are released into the cytosol and thereby contribute to the greater glycolytic capacity. Phinney *et al.* demonstrated that MSC-derived EVs significantly increased basal and maximum OCR in the recipient macrophages compared to controls in MSC-macrophage cocultures (39). Transfer of only a few mitochondria, even partially depolarized mitochondria is sufficient to rescue cellular bioenergetics in mtDNA-depleted recipient cells (39, 74, 107). Overall, our

western blotting results (**Fig. S16**) and Mitotracker deep red studies (**Fig. 4**) confirmed the presence of mitochondrial proteins and functional mitochondria in EVs. m/lEV mitochondria-mediated increase in recipient cellular mitochondrial respiration at 72 h (**Fig. 8**) is likely explained by the greater transfer and colocalization of m/lEV (**Fig. 4-6, S8,9**) into primary human brain endothelial cells and the greater extent of increases in intracellular ATP (**Fig. 7a-c**). Our use of these orthogonal tools and observations demonstrate that m/lEV contain a greater load of functional mitochondria compared to sEV. Transfer and colocalization of m/lEV mitochondria within the recipient primary human brain endothelial cells take about 48 to 72 h and this mitochondrial uptake consequently results in increased cellular ATP levels, mitochondrial respiration, and glycolytic capacities.

Shi *et al.* demonstrated that endothelial overexpression of HSP27 in transgenic mice showed a significant and prolonged reduction in infarct volume compared to neuronal overexpression of HSP27 and saline-treated transgenic focal ischemic mice (9). HSP27 inhibits the actin polymerization, reduces the G-actin/F-actin ratio and consequently restores the tight junction integrity during ischemia/reperfusion (9, 10). Native HSP27 has a half-life of about 2 h (109) and is susceptible to protease and enzymatic degradation in plasma and physiological conditions (110). We used EVs as a natural carrier and PEG-DET as a synthetic carrier to deliver HSP27 into endothelial cells. The isoelectric point of human recombinant HSP27 is 5.89 (43), therefore, it exerts a net negative charge at physiological pH 7.4 (**Fig. 10a**). Diethyltriamine side chain of PEG-DET cationic diblock copolymer has two pKa values associated with its molecular conformation (*gauche vs. anti*). The *gauche* conformation of DET exerts a pKa of 9.9 that induces the formation of stable complexes with negatively charged nucleotides at physiological

pH 7.4 (25, 111). We confirmed the formation of PEG-DET/HSP27 complexes using native PAGE followed by Coomassie staining (**Fig. 9a,b**) and dynamic light scattering (**Fig. 10a-c**). The optimal PEG-DET/HSP27 w/w ratio of 20/1 formed a complex with about 70% of HSP27 incorporation which was further confirmed by the disappearance of the HSP27 band in native PAGE (**Fig. 9a**) and a shift in the zeta potential from ca. -9 mV (HSP27) to about +9 mV (PEG-DET/HSP27 complexes) (**Fig. 10c**). These nano-sized complexes showed unimodal and narrow particle size distribution further confirming formation of complexes in the solution.

Despite the negative surface charge of EVs and the native HSP27 protein at pH 7.4, hCMEC/D3-EV/HSP27 mixtures showed about 20% protein interaction in native PAGE analysis. Haney *et al.* also reported that macrophage-derived exosomes incubated with bovine liver catalase proteins did not affect the particle diameter and dispersity indices of the EXO/catalase mixture (112). Notably, the zeta potential of EV/HSP27 mixtures was significantly different compared to native HSP27. The weaker interactions of HSP27 with EVs were advantageous for our study as we wanted to avoid any mode of intrusive cargo loading (such as sonication, freeze/thaw cycles, saponin-mediated loading) that may damage the integrity of EV membranes and inversely impact the functionality of innate cargo, specifically, their mitochondrial load. We further confirmed the m/lEV and HSP27 interactions using an immunoprecipitation pull-down assay (**Fig. S18**). We engineered ternary mixtures of EVs with PEG-DET/HSP27 complexes at different w/w ratios to increase the HSP27 loading into hCMEC/D3-derived EVs. The positively-charged PEG-DET/HSP27 complexes (+9 mV, **Fig. 10c**) formed an electrostatic complex with sEV and m/lEV which was confirmed by an intermediate HSP7 band density between PEG-DET/HSP27 complexes and sEV/HSP27

mixtures (**Fig. 9h**) and increased resulting particle diameters (**Fig. 10d**). (PEG-DET/HSP27)/EV complexes showed an electroneutral or slight-positive zeta potential (**Fig. 10f**) which may allow longer systemic circulation and a greater cellular uptake. The inclusion of EVs in (PEG-DET/HSP27)/EV complexes may facilitate interactions with the BBB and mediate endothelial targeting (114) during *in vivo* delivery while the positive charges derived from PEG-DET can enhance the cellular uptake and facilitate endosomal escape of HSP27 (25). The cytosolic release of HSP27 in endothelial cells can reduce the paracellular permeability of hydrophilic molecules and immune cells (9) and ultimately protect the BBB integrity.

We evaluated the prophylactic PEG-DET/HSP27 and EV/HSP27 treatment-induced protection of tight junction integrity by measuring the diffusion rate of the hydrophilic tracers. We used fluorescent tracers varying in molecular mass: we used 65-85 kDa TRITC-Dextran, a large molecular weight tracer to simulate the infiltration of proteins and blood-borne large molecules and 4.4 kDa TRITC-Dextran to simulate the diffusion of small molecules during ischemia/reperfusion. The diffusion rate of the larger 65-85 kD TRITC-Dextran in untreated hCMEC/D3 cells and HBMECs were compared at pre-OGD conditions, during OGD, and OGD/reperfusion conditions (**Fig. S19**). The baseline diffusion rate was found to be different for both cell models. The diffusion rate gradually increased and was relatively higher for the hCMEC/D3 cell line compared to the HBMEC monolayer during ischemia/reperfusion suggesting the inherent leakiness of the hCMEC/D3 cell line compared to primary HBMECs. Therefore, we studied the effects of naïve EV and HSP27 complexes on the diffusion rate of 4.4 kD and 65-85 kD TRITC-dextran during OGD and OGD/RP conditions in primary HBMEC monolayers. Naïve EVs, PEG-DET/HSP27, and EV/HSP27 complexes were cytocompatible

with HBMECs for 72 h of exposure under normoxic conditions (**Fig. 14a**). Notably, sEV/HSP27, m/lEV/HSP27, and EV/HSP27 mixtures significantly increased cell viability compared to untreated cells and are likely an additive effect of naïve EV mitochondrial transfer and anti-apoptotic/cell proliferation effects of HSP27 (115-118).

First, we analyzed the effects of naïve EV, PEG-DET/HSP27 complexes, and EV/HSP27 mixtures on the diffusion rate of 65-85 kD TRITC-Dextran. Exposure to the different treatment groups for 72 h did not affect the baseline permeability of HBMECs for large molecules. However, sEV/HSP27 mixtures showed an effect on limiting diffusion of the TRITC-Dextran (**Fig. 11a**). Interestingly, HBMECs treated with PEG-DET/HSP27 complexes efficiently decreased 65-85 kD TRITC-Dextran diffusion rate for 6 h of OGD exposure followed by an immediate hour of ischemia/reperfusion compared to OGD-HBMEC control, native HSP27, and free PEG-DET-treated groups (**Fig. 11b-f**). These results indicated that PEG-DET-mediated efficient transfer of HSP27 in endothelial cells could restore the integrity of tight junctions and protect the BBB during ischemia and ischemia/reperfusion injury. Importantly, naïve sEV and m/lEV-treated HBMECs showed strong BBB protection during OGD conditions and the first hour of ischemia/reperfusion.

It should be noted that naïve sEV also contain HSP proteins such as HSP20, HSP27, HSP40, and HSP70 (119-122), and therefore, the innate HSP load in sEV and m/lEV mitochondria may enhance overall endothelial cell survival and tight junction integrity during OGD conditions. EV/HSP27 mixtures further strengthened the endothelial tight junctions demonstrating that EV facilitates HSP27 transfer into the cells resulting in synergistic BBB protection from large

molecule infiltration during ischemia/reperfusion injury. We inferred that the tight junction integrity was restored after 2 h of reperfusion due to similar dextran diffusion rates in OGD, control, and treatment groups. Therefore, it is essential to protect endothelial tight junction integrity during the early stage of ischemia/reperfusion (<2 h in culture conditions). Importantly, PEG-DET/HSP27, EV/HSP27, and naïve EV-mediated protection of tight junction integrity during the early reperfusion stage allude to their promising role in ischemic stroke therapy. Lastly, we further confirmed the naïve EV, PEG-DET/HSP27, and EV/HSP27-induced protection of tight junction integrity against the paracellular flux of small molecules under OGD and OGD/reperfusion conditions. PEG-DET/HSP27 complexes strengthened the tight junctions to restrict 4.4 kD dextran entry up until 4 h of OGD exposure and an immediate hour of OGD/ reperfusion (**Fig. 12a-f**). Importantly, naïve EVs, but not their HSP27 complexes, retarded small molecule permeability during OGD conditions. Furthermore, naïve EV and their HSP27 complexes reduced 4.4 kD dextran diffusion during 6 h of ischemia/reperfusion injury. Notably, the magnitude of EV/HSP27 complex-mediated protection is considerably greater than naïve EVs demonstrating a synergistic effect of EVs and HSP27 in increasing endothelial tight junction integrity. Noteworthy, naïve EV and EV/HSP27 complexes-mediated reduction in 4.4 kD and 65-85 kD dextran diffusion rate were significantly higher and prolonged compared to polymer-based HSP27 delivery (**Fig. 11,12**).

To summarize, endothelial cell-derived naïve m/lEV contain functional mitochondria and sEV contains mitochondrial proteins that internalize and integrate with the mitochondrial network of recipient endothelial cells. As a result, naïve m/lEV and sEV increased ATP levels (albeit m/lEV showed a greater magnitude of ATP increases), mitochondrial respiration, and

glycolytic capacities in the recipient brain endothelial cells. EV/HSP27 mixtures restored tight junction integrity in primary human brain endothelial cells by limiting the paracellular permeability of small and large molar mass tracer molecules during ischemia/reperfusion injury.

Our future *in vivo* studies will determine the pharmacokinetic profile, biodistribution, and therapeutic efficacy of HSP27-m/lEV in a mouse model of stroke. ^{125}I-radiolabeled m/lEVs will be administered intravenously to CD-1 mice to determine their serum and whole brain PK parameters such as circulation $t_{1/2}$, clearance, blood-to-brain unidirectional influx constant, and brain-to-blood efflux rate (2). We will then determine whether post-ischemic administration of an optimal m/lEV dose protects the BBB and improves histological and functional outcomes.

5. Conclusion

This one-two punch approach increased the brain endothelial cell survival and their mitochondrial function due to the innate EV mitochondrial load, and EV/HSP27 restored BBB tight junction integrity by limiting the paracellular permeability of small and large molecular mass tracers. The outcome of the present study indicates that this approach has potential to protect the BBB *in vivo* that in turn can ameliorate the long-term neurological damage and dysfunction in rodent models of ischemic stroke.

Acknowledgments

This work was supported via start-up funds for the Manickam laboratory from Duquesne University (DU) and a 2021 Faculty Development Fund (Office of Research, DU) to the PI. We

would like to acknowledge the Neurodegenerative Undergraduate Research Experience (NURE) R25NS100118 for funding DXD. The authors express their deep appreciation to Dr. Rehana Leak (DU) for her brilliant insights and technical advice. The authors are thankful to Dr. Lauren O'Donnell, and Mss. Manisha Chandwani and Yashika Kamte (DU) for flow cytometry support.

References

1. https://www.cdc.gov/stroke/facts.htm
2. Nian K, Harding IC, Herman IM, Ebong EE. Blood-Brain Barrier Damage in Ischemic Stroke and Its Regulation by Endothelial Mechanotransduction. Front Physiol. 2020;11(1681).
3. Abdullahi W, Tripathi D, Ronaldson PT. Blood-brain barrier dysfunction in ischemic stroke: targeting tight junctions and transporters for vascular protection. Am J Physiol Cell Physiol. 2018;315(3):C343-C56.
4. Bernardo-Castro S, Sousa JA, Brás A, Cecília C, Rodrigues B, Almendra L, et al. Pathophysiology of Blood–Brain Barrier Permeability Throughout the Different Stages of Ischemic Stroke and Its Implication on Hemorrhagic Transformation and Recovery. Frontiers in Neurology. 2020;11(1605).
5. Liu S, Feng X, Jin R, Li G. Tissue plasminogen activator-based nanothrombolysis for ischemic stroke. Expert Opin Drug Deliv. 2018;15(2):173-84.
6. Zhang Y, Wang Y, Zuo Z, Wang Z, Roy J, Hou Q, et al. Effects of tissue plasminogen activator timing on blood-brain barrier permeability and hemorrhagic transformation in rats with transient ischemic stroke. J Neurol Sci. 2014;347(1-2):148-54.
7. Jiang X, Andjelkovic AV, Zhu L, Yang T, Bennett MVL, Chen J, et al. Blood-brain barrier dysfunction and recovery after ischemic stroke. Prog Neurobiol. 2018;163-164:144-71.
8. Stamatovic SM, Keep RF, Wang MM, Jankovic I, Andjelkovic AV. Caveolae-mediated internalization of occludin and claudin-5 during CCL2-induced tight junction remodeling in brain endothelial cells. J Biol Chem. 2009;284(28):19053-66.
9. Shi Y, Jiang X, Zhang L, Pu H, Hu X, Zhang W, et al. Endothelium-targeted overexpression of heat shock protein 27 ameliorates blood-brain barrier disruption after ischemic brain injury. Proc Natl Acad Sci U S A. 2017;114(7):E1243-E52.
10. Leak RK, Zhang L, Stetler RA, Weng Z, Li P, Atkins GB, et al. HSP27 protects the blood-brain barrier against ischemia-induced loss of integrity. CNS Neurol Disord Drug Targets. 2013;12(3):325-37.
11. Rada CC, Mejia-Pena H, Grimsey NJ, Cordova IC, Olson J, Wozniak JM, et al. Heat shock protein 27 activity is linked to endothelial barrier recovery after proinflammatory GPCR-induced disruption. Sci Signal. 2021;14(698):eabc1044.
12. During RL, Gibson BG, Li W, Bishai EA, Sidhu GS, Landry J, et al. Anthrax lethal toxin paralyzes actin-based motility by blocking Hsp27 phosphorylation. EMBO J. 2007;26(9):2240-50.

13. Hirano S, Rees RS, Yancy SL, Welsh MJ, Remick DG, Yamada T, et al. Endothelial barrier dysfunction caused by LPS correlates with phosphorylation of HSP27 in vivo. Cell Biol Toxicol. 2004;20(1):1-14.
14. Miron T, Vancompernolle K, Vandekerckhove J, Wilchek M, Geiger B. A 25-kD inhibitor of actin polymerization is a low molecular mass heat shock protein. J Cell Biol. 1991;114(2):255-61.
15. Jakob U, Gaestel M, Engel K, Buchner J. Small heat shock proteins are molecular chaperones. J Biol Chem. 1993;268(3):1517-20.
16. Garrido C, Bruey JM, Fromentin A, Hammann A, Arrigo AP, Solary E. HSP27 inhibits cytochrome c-dependent activation of procaspase-9. FASEB J. 1999;13(14):2061-70.
17. Voss OH, Batra S, Kolattukudy SJ, Gonzalez-Mejia ME, Smith JB, Doseff AI. Binding of caspase-3 prodomain to heat shock protein 27 regulates monocyte apoptosis by inhibiting caspase-3 proteolytic activation. J Biol Chem. 2007;282(34):25088-99.
18. Bruey JM, Ducasse C, Bonniaud P, Ravagnan L, Susin SA, Diaz-Latoud C, et al. Hsp27 negatively regulates cell death by interacting with cytochrome c. Nat Cell Biol. 2000;2(9):645-52.
19. D'Souza A, Burch A, Dave KM, Sreeram A, Reynolds MJ, Dobbins DX, et al. Microvesicles transfer mitochondria and increase mitochondrial function in brain endothelial cells. J Control Release. 2021;338:505-26.
20. Banks WA, Sharma P, Bullock KM, Hansen KM, Ludwig N, Whiteside TL. Transport of Extracellular Vesicles across the Blood-Brain Barrier: Brain Pharmacokinetics and Effects of Inflammation. International journal of molecular sciences. 2020;21(12):4407.
21. Murphy DE, de Jong OG, Brouwer M, Wood MJ, Lavieu G, Schiffelers RM, et al. Extracellular vesicle-based therapeutics: natural versus engineered targeting and trafficking. Experimental & Molecular Medicine. 2019;51(3):1-12.
22. Doyle LM, Wang MZ. Overview of Extracellular Vesicles, Their Origin, Composition, Purpose, and Methods for Exosome Isolation and Analysis. Cells. 2019;8(7):727.
23. Théry C, Witwer KW, Aikawa E, Alcaraz MJ, Anderson JD, Andriantsitohaina R, et al. Minimal information for studies of extracellular vesicles 2018 (MISEV2018): a position statement of the International Society for Extracellular Vesicles and update of the MISEV2014 guidelines. Journal of Extracellular Vesicles. 2018;7(1):1535750.
24. He Z, Ning N, Zhou Q, Khoshnam SE, Farzaneh M. Mitochondria as a therapeutic target for ischemic stroke. Free Radical Biology and Medicine. 2020;146:45-58.
25. Jiang Y, Arounleut P, Rheiner S, Bae Y, Kabanov AV, Milligan C, et al. SOD1 nanozyme with reduced toxicity and MPS accumulation. J Control Release. 2016;231:38-49.
26. Han M, Bae Y, Nishiyama N, Miyata K, Oba M, Kataoka K. Transfection study using multicellular tumor spheroids for screening non-viral polymeric gene vectors with low cytotoxicity and high transfection efficiencies. Journal of Controlled Release. 2007;121(1):38-48.
27. Xiong MP, Bae Y, Fukushima S, Forrest ML, Nishiyama N, Kataoka K, et al. pH-Responsive Multi-PEGylated Dual Cationic Nanoparticles Enable Charge Modulations for Safe Gene Delivery. ChemMedChem. 2007;2(9):1321-7.
28. Lai TC, Bae Y, Yoshida T, Kataoka K, Kwon GS. pH-Sensitive Multi-PEGylated Block Copolymer as a Bioresponsive pDNA Delivery Vector. Pharmaceutical Research. 2010;27(11):2260-73.

29. Dave KM, Zhao W, Hoover C, D'Souza A, S Manickam D. Extracellular Vesicles Derived from a Human Brain Endothelial Cell Line Increase Cellular ATP Levels. AAPS PharmSciTech. 2021;22(1):18.
30. Chen TH, Bae Y, Furgeson DY, Kwon GS. Biodegradable hybrid recombinant block copolymers for non-viral gene transfection. Int J Pharm. 2012;427(1):105-12.
31. Kanayama N, Fukushima S, Nishiyama N, Itaka K, Jang W-D, Miyata K, et al. A PEG-Based Biocompatible Block Catiomer with High Buffering Capacity for the Construction of Polyplex Micelles Showing Efficient Gene Transfer toward Primary Cells. ChemMedChem. 2006;1(4):439-44.
32. Donker RB, Mouillet JF, Chu T, Hubel CA, Stolz DB, Morelli AE, et al. The expression profile of C19MC microRNAs in primary human trophoblast cells and exosomes. Mol Hum Reprod. 2012;18(8):417-24.
33. Hough KP, Trevor JL, Strenkowski JG, Wang Y, Chacko BK, Tousif S, et al. Exosomal transfer of mitochondria from airway myeloid-derived regulatory cells to T cells. Redox Biol. 2018;18(2213-2317):54-64.
34. Dave KM, Ali L, Manickam DS. Characterization of the SIM-A9 cell line as a model of activated microglia in the context of neuropathic pain. PLOS ONE. 2020;15(4):e0231597.
35. Dave KM, Han L, Jackson MA, Kadlecik L, Duvall CL, D SM. DNA Polyplexes of a Phosphorylcholine-Based Zwitterionic Polymer for Gene Delivery. Pharm Res. 2020;37(9):176.
36. Dai X, Chen J, Xu F, Zhao J, Cai W, Sun Z, et al. TGFalpha preserves oligodendrocyte lineage cells and improves white matter integrity after cerebral ischemia. J Cereb Blood Flow Metab. 2020;40(3):639-55.
37. Cardenes N, Corey C, Geary L, Jain S, Zharikov S, Barge S, et al. Platelet bioenergetic screen in sickle cell patients reveals mitochondrial complex V inhibition, which contributes to platelet activation. Blood. 2014;123(18):2864-72.
38. Anne Stetler R, Leak RK, Gao Y, Chen J. The dynamics of the mitochondrial organelle as a potential therapeutic target. Journal of cerebral blood flow and metabolism : official journal of the International Society of Cerebral Blood Flow and Metabolism. 2013;33(1):22-32.
39. Phinney DG, Di Giuseppe M, Njah J, Sala E, Shiva S, St Croix CM, et al. Mesenchymal stem cells use extracellular vesicles to outsource mitophagy and shuttle microRNAs. Nature Communications. 2015;6(1):8472.
40. Todkar K, Chikhi L, Desjardins V, El-Mortada F, Pépin G, Germain M. Selective packaging of mitochondrial proteins into extracellular vesicles prevents the release of mitochondrial DAMPs. Nature Communications. 2021;12(1):1971.
41. CellLight™ Mitochondria-GFP, BacMam 2.0 (ThermoFisher website) [
42. https://www.agilent.com/en/products/cell-analysis/how-seahorse-xf-analyzers-work. [
43. http://protcalc.sourceforge.net/. [
44. Venkat P, Chopp M, Chen J. Blood-Brain Barrier Disruption, Vascular Impairment, and Ischemia/Reperfusion Damage in Diabetic Stroke. J Am Heart Assoc. 2017;6(6):e005819.
45. Arba F, Rinaldi C, Caimano D, Vit F, Busto G, Fainardi E. Blood-Brain Barrier Disruption and Hemorrhagic Transformation in Acute Ischemic Stroke: Systematic Review and Meta-Analysis. Front Neurol. 2020;11:594613.
46. Shi Y, Zhang L, Pu H, Mao L, Hu X, Jiang X, et al. Rapid endothelial cytoskeletal reorganization enables early blood–brain barrier disruption and long-term ischaemic reperfusion brain injury. Nature Communications. 2016;7(1):10523.

47. Shimada Y, Shimura H, Tanaka R, Yamashiro K, Koike M, Uchiyama Y, et al. Phosphorylated recombinant HSP27 protects the brain and attenuates blood-brain barrier disruption following stroke in mice receiving intravenous tissue-plasminogen activator. PLOS ONE. 2018;13(5):e0198039.
48. Falchi AM, Sogos V, Saba F, Piras M, Congiu T, Piludu M. Astrocytes shed large membrane vesicles that contain mitochondria, lipid droplets and ATP. Histochem Cell Biol. 2013;139(2):221-31.
49. Puhm F, Afonyushkin T, Resch U, Obermayer G, Rohde M, Penz T, et al. Mitochondria Are a Subset of Extracellular Vesicles Released by Activated Monocytes and Induce Type I IFN and TNF Responses in Endothelial Cells. Circulation Research. 2019;125(1):43-52.
50. El Andaloussi S, Mäger I, Breakefield XO, Wood MJA. Extracellular vesicles: biology and emerging therapeutic opportunities. Nature Reviews Drug Discovery. 2013;12(5):347-57.
51. Oldendorf WH, Cornford ME, Brown WJ. The large apparent work capability of the blood-brain barrier: a study of the mitochondrial content of capillary endothelial cells in brain and other tissues of the rat. Ann Neurol. 1977;1(5):409-17.
52. Schiera G, Di Liegro CM, Di Liegro I. Extracellular Membrane Vesicles as Vehicles for Brain Cell-to-Cell Interactions in Physiological as well as Pathological Conditions. BioMed Research International. 2015;2015:152926.
53. Andras IE, Toborek M. Extracellular vesicles of the blood-brain barrier. Tissue Barriers. 2016;4(1):e1131804.
54. Yang T, Martin P, Fogarty B, Brown A, Schurman K, Phipps R, et al. Exosome delivered anticancer drugs across the blood-brain barrier for brain cancer therapy in Danio rerio. Pharm Res. 2015;32(6):2003-14.
55. Yang D, Zhang W, Zhang H, Zhang F, Chen L, Ma L, et al. Progress, opportunity, and perspective on exosome isolation - efforts for efficient exosome-based theranostics. Theranostics. 2020;10(8):3684-707.
56. Dozio V, Sanchez JC. Characterisation of extracellular vesicle-subsets derived from brain endothelial cells and analysis of their protein cargo modulation after TNF exposure. J Extracell Vesicles. 2017;6(1):1302705.
57. Kanada M, Bachmann MH, Hardy JW, Frimannson DO, Bronsart L, Wang A, et al. Differential fates of biomolecules delivered to target cells via extracellular vesicles. Proceedings of the National Academy of Sciences. 2015;112(12):E1433-E42.
58. Konoshenko MY, Lekchnov EA, Vlassov AV, Laktionov PP. Isolation of Extracellular Vesicles: General Methodologies and Latest Trends. Biomed Res Int. 2018;2018:8545347.
59. Jeyaram A, Jay SM. Preservation and Storage Stability of Extracellular Vesicles for Therapeutic Applications. AAPS J. 2017;20(1):1.
60. Ge Q, Zhou Y, Lu J, Bai Y, Xie X, Lu Z. miRNA in Plasma Exosome is Stable under Different Storage Conditions. Molecules. 2014;19(2):1568-75.
61. Witwer KW, Buzás EI, Bemis LT, Bora A, Lässer C, Lötvall J, et al. Standardization of sample collection, isolation and analysis methods in extracellular vesicle research. J Extracell Vesicles. 2013;2(1):20360.
62. Lőrincz ÁM, Timár CI, Marosvári KA, Veres DS, Otrokocsi L, Kittel Á, et al. Effect of storage on physical and functional properties of extracellular vesicles derived from neutrophilic granulocytes. J Extracell Vesicles. 2014;3(1):25465.
63. Gray WD, Mitchell AJ, Searles CD. An accurate, precise method for general labeling of extracellular vesicles. MethodsX. 2015;2:360-7.

64. Kong F, Zhang L, Wang H, Yuan G, Guo A, Li Q, et al. Impact of collection, isolation and storage methodology of circulating microvesicles on flow cytometric analysis. Exp Ther Med. 2015;10(6):2093-101.
65. Mitchell PJ, Welton J, Staffurth J, Court J, Mason MD, Tabi Z, et al. Can urinary exosomes act as treatment response markers in prostate cancer? J Transl Med. 2009;7:4.
66. Goldberg J, Currais A, Prior M, Fischer W, Chiruta C, Ratliff E, et al. The mitochondrial ATP synthase is a shared drug target for aging and dementia. Aging Cell. 2018;17(2):e12715.
67. Jonckheere AI, Smeitink JAM, Rodenburg RJT. Mitochondrial ATP synthase: architecture, function and pathology. Journal of Inherited Metabolic Disease. 2012;35(2):211-25.
68. Andreu Z, Yáñez-Mó M. Tetraspanins in extracellular vesicle formation and function. Front Immunol. 2014;5:442.
69. Zhang Y, Tan J, Miao Y, Zhang Q. The effect of extracellular vesicles on the regulation of mitochondria under hypoxia. Cell Death & Disease. 2021;12(4):358.
70. Park JH, Hayakawa K. Extracellular Mitochondria Signals in CNS Disorders. Front Cell Dev Biol. 2021;9(248):642853.
71. Liu D, Gao Y, Liu J, Huang Y, Yin J, Feng Y, et al. Intercellular mitochondrial transfer as a means of tissue revitalization. Signal Transduct Target Ther. 2021;6(1):65.
72. Rutkai I, Merdzo I, Wunnava SV, Curtin GT, Katakam PV, Busija DW. Cerebrovascular function and mitochondrial bioenergetics after ischemia-reperfusion in male rats. J Cereb Blood Flow Metab. 2019;39(6):1056-68.
73. Ikeda G, Santoso MR, Tada Y, Li AM, Vaskova E, Jung J-H, et al. Mitochondria-Rich Extracellular Vesicles From Autologous Stem Cell–Derived Cardiomyocytes Restore Energetics of Ischemic Myocardium. Journal of the American College of Cardiology. 2021;77(8):1073-88.
74. Spees JL, Olson SD, Whitney MJ, Prockop DJ. Mitochondrial transfer between cells can rescue aerobic respiration. Proceedings of the National Academy of Sciences. 2006;103(5):1283-8.
75. Islam MN, Das SR, Emin MT, Wei M, Sun L, Westphalen K, et al. Mitochondrial transfer from bone-marrow–derived stromal cells to pulmonary alveoli protects against acute lung injury. Nature Medicine. 2012;18(5):759-65.
76. Hayakawa K, Esposito E, Wang X, Terasaki Y, Liu Y, Xing C, et al. Transfer of mitochondria from astrocytes to neurons after stroke. Nature. 2016;535(7613):551-5.
77. Sinha P, Islam MN, Bhattacharya S, Bhattacharya J. Intercellular mitochondrial transfer: bioenergetic crosstalk between cells. Current Opinion in Genetics & Development. 2016;38:97-101.
78. Gao L, Zhang Z, Lu J, Pei G. Mitochondria Are Dynamically Transferring Between Human Neural Cells and Alexander Disease-Associated GFAP Mutations Impair the Astrocytic Transfer. Front Cell Neurosci. 2019;13(316):316.
79. Guescini M, Genedani S, Stocchi V, Agnati LF. Astrocytes and Glioblastoma cells release exosomes carrying mtDNA. Journal of Neural Transmission. 2009;117(1):1.
80. Xiao B, Deng X, Zhou W, Tan EK. Flow Cytometry-Based Assessment of Mitophagy Using MitoTracker. Front Cell Neurosci. 2016;10(76):76.
81. Chazotte B. Labeling mitochondria with MitoTracker dyes. Cold Spring Harb Protoc. 2011;2011(8):990-2.
82. Mulcahy LA, Pink RC, Carter DR. Routes and mechanisms of extracellular vesicle uptake. J Extracell Vesicles. 2014;3(2001-3078).

83. Costa Verdera H, Gitz-Francois JJ, Schiffelers RM, Vader P. Cellular uptake of extracellular vesicles is mediated by clathrin-independent endocytosis and macropinocytosis. J Control Release. 2017;266:100-8.
84. Cronqvist T, Erlandsson L, Tannetta D, Hansson SR. Placental syncytiotrophoblast extracellular vesicles enter primary endothelial cells through clathrin-mediated endocytosis. Placenta. 2020;100:133-41.
85. Mohning MP, Thomas SM, Barthel L, Mould KJ, McCubbrey AL, Frasch SC, et al. Phagocytosis of microparticles by alveolar macrophages during acute lung injury requires MerTK. Am J Physiol Lung Cell Mol Physiol. 2018;314(1):L69-l82.
86. van Niel G, D'Angelo G, Raposo G. Shedding light on the cell biology of extracellular vesicles. Nat Rev Mol Cell Biol. 2018;19(4):213-28.
87. Parolini I, Federici C, Raggi C, Lugini L, Palleschi S, De Milito A, et al. Microenvironmental pH is a key factor for exosome traffic in tumor cells. J Biol Chem. 2009;284(49):34211-22.
88. Montecalvo A, Larregina AT, Shufesky WJ, Stolz DB, Sullivan ML, Karlsson JM, et al. Mechanism of transfer of functional microRNAs between mouse dendritic cells via exosomes. Blood. 2012;119(3):756-66.
89. Cronqvist T, Tannetta D, Mörgelin M, Belting M, Sargent I, Familari M, et al. Syncytiotrophoblast derived extracellular vesicles transfer functional placental miRNAs to primary human endothelial cells. Scientific Reports. 2017;7(1):4558.
90. Santos MF, Rappa G, Karbanová J, Kurth T, Corbeil D, Lorico A. VAMP-associated protein-A and oxysterol-binding protein-related protein 3 promote the entry of late endosomes into the nucleoplasmic reticulum. J Biol Chem. 2018;293(36):13834-48.
91. Petty RD, Sutherland LA, Hunter EM, Cree IA. Comparison of MTT and ATP-based assays for the measurement of viable cell number. J Biolumin Chemilumin. 1995;10(1):29-34.
92. Guo Y, Chi X, Wang Y, Heng BC, Wei Y, Zhang X, et al. Mitochondria transfer enhances proliferation, migration, and osteogenic differentiation of bone marrow mesenchymal stem cell and promotes bone defect healing. Stem Cell Res Ther. 2020;11(1):245.
93. Zhang J, Tan Z, Tran ND. Chemical hypoxia-ischemia induces apoptosis in cerebromicrovascular endothelial cells. Brain Res. 2000;877(2):134-40.
94. Andjelkovic AV, Xiang J, Stamatovic SM, Hua Y, Xi G, Wang MM, et al. Endothelial Targets in Stroke. Arteriosclerosis, Thrombosis, and Vascular Biology. 2019;39(11):2240-7.
95. Yang DI, Lin TN, Yin KJ, Hu CJ, Chen SD, Xu J, et al. Cerebral Endothelial Cell Reaction to Ischemic Insults. In: Lajtha A, Chan PH, editors. Handbook of Neurochemistry and Molecular Neurobiology: Acute Ischemic Injury and Repair in the Nervous System. Boston, MA: Springer US; 2007. p. 165-83.
96. Keep R.F. AAV, Stamatovic S.M., Shakui P., Ennis S.R. Ischemia-induced endothelial cell dysfunction. Intracranial Pressure and Brain Monitoring XII. 2005;95.
97. Park H-H, Han M-H, Choi H, Lee YJ, Kim JM, Cheong JH, et al. Mitochondria damaged by Oxygen Glucose Deprivation can be Restored through Activation of the PI3K/Akt Pathway and Inhibition of Calcium Influx by Amlodipine Camsylate. Scientific Reports. 2019;9(1):15717.
98. Liao L-X, Zhao M-B, Dong X, Jiang Y, Zeng K-W, Tu P-F. TDB protects vascular endothelial cells against oxygen-glucose deprivation/reperfusion-induced injury by targeting miR-34a to increase Bcl-2 expression. Scientific Reports. 2016;6(1):37959.

99. Kong LY, Liang MY, Liu JP, Lai P, Ye JS, Zhang ZX, et al. Mesenchymal Stem Cell-derived Exosomes Rescue Oxygen-Glucose Deprivation-induced Injury in Endothelial Cells. Curr Neurovasc Res. 2020;17(2):155-63.
100. Arslan F, Lai RC, Smeets MB, Akeroyd L, Choo A, Aguor ENE, et al. Mesenchymal stem cell-derived exosomes increase ATP levels, decrease oxidative stress and activate PI3K/Akt pathway to enhance myocardial viability and prevent adverse remodeling after myocardial ischemia/reperfusion injury. Stem Cell Research. 2013;10(3):301-12.
101. Pasquale D'Acunzo oP-G, Yohan Kim, Tal Hargash, Chelsea Miller, Melissa J. Alldred, Hediye Erdjument-Bromage, Sai C. Penikalapati, Monika Pawlik, Mitsuo Saito, Mariko Saito, Stephen D. Ginsberg, Thomas A. Neubert, Chris N. Goulbourne, Efrat Levy. Mitovesicles are a novel population of extracellular vesicles of mitochondrial origin altered in Down syndrome. Scientific Reports. 2021;7:eabe5085
102. Yetkin-Arik B, Vogels IMC, Nowak-Sliwinska P, Weiss A, Houtkooper RH, Van Noorden CJF, et al. The role of glycolysis and mitochondrial respiration in the formation and functioning of endothelial tip cells during angiogenesis. Scientific Reports. 2019;9(1):12608.
103. Smolina N, Bruton J, Kostareva A, Sejersen T. Assaying Mitochondrial Respiration as an Indicator of Cellular Metabolism and Fitness. Methods Mol Biol. 2017;1601:79-87.
104. Rose S, Frye RE, Slattery J, Wynne R, Tippett M, Pavliv O, et al. Oxidative stress induces mitochondrial dysfunction in a subset of autism lymphoblastoid cell lines in a well-matched case control cohort. PLoS One. 2014;9(1):e85436.
105. Wang Z, Guan D, Wang S, Chai LYA, Xu S, Lam KP. Glycolysis and Oxidative Phosphorylation Play Critical Roles in Natural Killer Cell Receptor-Mediated Natural Killer Cell Functions. Front Immunol. 2020;11(202):202.
106. GM C. The Mechanism of Oxidative Phosphorylation. The Cell: A Molecular Approach. 2. Sunderland (MA): Sinauer Associates; 2000.
107. King MP, Attardi G. Injection of mitochondria into human cells leads to a rapid replacement of the endogenous mitochondrial DNA. Cell. 1988;52(6):811-9.
108. Kadry H, Noorani B, Cucullo L. A blood–brain barrier overview on structure, function, impairment, and biomarkers of integrity. Fluids and Barriers of the CNS. 2020;17(1):69.
109. Li D, Duncan RF. Transient acquired thermotolerance in Drosophila, correlated with rapid degradation of Hsp70 during recovery. Eur J Biochem. 1995;231(2):454-65.
110. Zimmermann M, Traxler D, Simader E, Bekos C, Dieplinger B, Lainscak M, et al. In vitro Stability of Heat Shock Protein 27 in Serum and Plasma Under Different Pre-analytical Conditions: Implications for Large-Scale Clinical Studies. Ann Lab Med. 2016;36(4):353-7.
111. Miyata K, Oba M, Nakanishi M, Fukushima S, Yamasaki Y, Koyama H, et al. Polyplexes from Poly(aspartamide) Bearing 1,2-Diaminoethane Side Chains Induce pH-Selective, Endosomal Membrane Destabilization with Amplified Transfection and Negligible Cytotoxicity. Journal of the American Chemical Society. 2008;130(48):16287-94.
112. Haney MJ, Klyachko NL, Zhao Y, Gupta R, Plotnikova EG, He Z, et al. Exosomes as drug delivery vehicles for Parkinson's disease therapy. J Control Release. 2015;207:18-30.
113. Ramasubramanian L, Kumar P, Wang A. Engineering Extracellular Vesicles as Nanotherapeutics for Regenerative Medicine. Biomolecules. 2019;10(1):48.
114. Yuan D, Zhao Y, Banks WA, Bullock KM, Haney M, Batrakova E, et al. Macrophage exosomes as natural nanocarriers for protein delivery to inflamed brain. Biomaterials. 2017;142:1-12.

115. Zhang S, Hu Y, Huang Y, Xu H, Wu G, Dai H. Heat shock protein 27 promotes cell proliferation through activator protein-1 in lung cancer. Oncol Lett. 2015;9(6):2572-6.
116. Park A-M, Tsunoda I, Yoshie O. Heat shock protein 27 promotes cell cycle progression by down-regulating E2F transcription factor 4 and retinoblastoma family protein p130. J Biol Chem. 2018;293(41):15815-26.
117. Stetler RA, Gao Y, Signore AP, Cao G, Chen J. HSP27: mechanisms of cellular protection against neuronal injury. Curr Mol Med. 2009;9(7):863-72.
118. Venugopal A, Sundaramoorthy K, Vellingiri B. Therapeutic potential of Hsp27 in neurological diseases. Egyptian Journal of Medical Human Genetics. 2019;20(1):21.
119. Reddy VS, Madala SK, Trinath J, Reddy GB. Extracellular small heat shock proteins: exosomal biogenesis and function. Cell Stress Chaperones. 2018;23(3):441-54.
120. Wyciszkiewicz A, Kalinowska-Łyszczarz A, Nowakowski B, Kaźmierczak K, Osztynowicz K, Michalak S. Expression of small heat shock proteins in exosomes from patients with gynecologic cancers. Scientific Reports. 2019;9(1):9817.
121. Chanteloup G, Cordonnier M, Isambert N, Bertaut A, Marcion G, Garrido C, et al. Membrane-bound exosomal HSP70 as a biomarker for detection and monitoring of malignant solid tumours: a pilot study. Pilot and Feasibility Studies. 2020;6(1):35.
122. Takeuchi T, Suzuki M, Fujikake N, Popiel HA, Kikuchi H, Futaki S, et al. Intercellular chaperone transmission via exosomes contributes to maintenance of protein homeostasis at the organismal level. Proceedings of the National Academy of Sciences. 2015;112(19):E2497-E506.